Thalamo-insular pathway regulates tic generation via motor-limbic crosstalk

Authors:

Hiroto Kuno,[1] Natsumi Tsuji,[1] Kenta Kobayashi,[2,3] Toru Takumi,[1] Yoshihisa Tachibana[1,4,*]

[1]Department of Physiology and Cell Biology, Kobe University Graduate School of Medicine, Kobe, Japan.

[2]Section of Viral Vector Development, National Institute for Physiological Sciences, Okazaki, Japan.

[3]Department of Physiological Sciences, SOKENDAI (The Graduate University for Advanced Studies), Okazaki, Japan.

[4]Lead contact

*Correspondence: yoshi@med.kobe-u.ac.jp

Corresponding author:

Dr. Yoshihisa Tachibana

Department of Physiology and Cell Biology,

Kobe University Graduate School of Medicine, Kobe, Japan.

7-5-1 Kusunoki-cho, Chuo-ku, Kobe, Hyogo 650-0017, Japan

Phone: +81-78-382-5832

E-mail: yoshi@med.kobe-u.ac.jp

Highlights:

1. c-Fos activation occurs in both motor and limbic structures in a mouse tic model
2. Basal ganglia outputs are transmitted to insula via intralaminar thalamic nuclei
3. Chemogenetic inhibition of thalamo-insular pathway suppresses motor tics
4. Thalamo-insular inhibition diminishes tic-associated activity in primary motor cortex

In brief:

Abnormal basal ganglia activity originating from the striatum drives dysfunction of the insular cortex via the intralaminar thalamic nuclei, leading to motor tics. Chemogenetic inhibition of this pathway suppresses tic-like behaviors, highlighting motor-limbic circuit pathology in tic disorders.

SUMMARY

Tic disorders accompanied by premonitory urges are hallmark symptoms of Tourette syndrome (TS), yet the underlying neuronal mechanisms remain elusive. Here, we establish a mouse model of motor tics by unilateral striatal injection of a $GABA_A$ receptor antagonist. This model induces c-Fos activation in both motor and limbic structures, including the insular cortex (IC). Fiber photometry reveals tic-associated activity in IC as well as the primary motor cortex (M1). Viral tracing demonstrates that basal ganglia outputs from the substantia nigra pars reticulata are transmitted to IC via the intralaminar thalamic nuclei (ITN). Chemogenetic inhibition of IC or the thalamo-insular pathway suppresses tic-related cortical activity and alleviates tic-like behaviors. These findings identify IC as a key node in tic generation and highlight ITN as critical relay stations linking motor and limbic circuits. Aberrant thalamo-insular signaling thus contributes to the pathophysiology of tic disorders and represents a potential therapeutic target in TS.

INTRODUCTION

Motor and vocal tics are characterized by sudden, rapid, repetitive movements or involuntary vocalizations.[1] These symptoms are often preceded by an uncomfortable sensation, known as a premonitory urge, which can be transiently relieved by tic expression.[2-5] Gilles de la Tourette syndrome (TS) is diagnosed by the presence of multiple motor tics and at least one vocal tic persisting for over a year,[1] and is frequently accompanied by comorbidities such as obsessive-compulsive disorder (OCD) and attention-deficit/hyperactivity disorder (ADHD).[6-8] TS typically begins in childhood, affecting approximately 0.3–1.0% of school-aged children.[1,9-12] While symptoms often improve during adolescence, they can persist or even worsen into adulthood.[1,6]

Current treatment strategies for TS patients include behavioral therapy, pharmacological agents, and, in severe cases, surgical interventions.[13] Despite extensive clinical characterization, however, the neuronal mechanisms driving tic generation remain incompletely understood. Accumulating evidence implicates dysfunction of the cortico-basal ganglia (BG)-thalamo-cortical (CBGTC) circuits in the pathophysiology of TS.[14] Microinjections of $GABA_A$ receptor antagonists into the sensorimotor striatum reliably induce motor tics in rats and monkeys.[15-19] Notably, similar manipulations in the associative or limbic subdivisions of the monkey striatum produce distinct behavioral phenotypes: hyperactive and impulsive behaviors resembling ADHD symptoms, or stereotyped behaviors reminiscent of OCD, respectively.[19] These findings support the "striatal disinhibition hypothesis", which posits that local GABAergic deficits underlie the pathophysiology of TS symptoms. The striatum contains diverse subtypes of GABAergic interneurons: parvalbumin (PV)-, calretinin-, and neuropeptide Y-positive neurons.[20] Postmortem studies have revealed a selective reduction of striatal GABAergic

interneurons in TS patients.[21,22] In parallel, the "hyperactive dopamine hypothesis" also provides a compelling framework since pharmacological interventions with dopamine receptor antagonists (i.e., antipsychotics) are clinically effective in suppressing tic symptoms in TS patients.[6,13,23] However, intrastriatal administration of dopamine agonists in rodents induces stereotyped behaviors, rather than motor tics.[24] Taken together, these findings highlight that striatal disinhibition-based animal models provide a mechanistically relevant approach for investigating the neuronal circuits underlying tic generation.

Here, we report that striatal injection of bicuculline, a $GABA_A$ receptor antagonist, induces motor tics in mice. This model induces activation in both motor and limbic structures, including the insular cortex (IC). We identify an output pathway from BG to IC via the intralaminar thalamic nuclei (ITN), and demonstrate that chemogenetic inhibition of this pathway alleviates tic-like behaviors. These results reveal a motor-limbic circuit that contributes to tic generation.

RESULTS

Unilateral striatal bicuculline injection induces tic-like movements

We established a mouse model of motor tics by unilateral injection of bicuculline, a $GABA_A$ receptor antagonist, at a low dose (0.2 μg/μl; 0.20 μl per injection) into the motor domain of the dorsal striatum (dSTR) in head-fixed mice (Figure 1). This paradigm recapitulates striatal disinhibition protocols (Figure S1A) previously shown to induce motor tics in rats and monkeys.[15-19] To monitor the tic-associated cortical activity, we simultaneously recorded electroencephalogram (EEG) signals from the primary motor cortex (M1) ipsilateral to the injection site, together with electromyogram (EMG) activity from the contralateral triceps muscle (Figure 1A). Bicuculline injection into the dSTR produced somatotopically organized tic-like movements in contralateral body parts (Figure S1B and Video S1), depending on the dorsoventral striatal level, as previously reported.[15,16] In this study, we targeted the striatal injection site (AP: 0.0 mm, ML: 2.7 mm, DV: 3.5 mm from the bregma; Figure 1B), which reliably induced tic-like movements mainly in the contralateral forelimb and orofacial regions (Figure S1B and Video S1). EEG spikes in M1 preceded EMG bursts and kinematic acceleration of the corresponding body parts (Figures 1C-1E for the wrist; S1C-S1E for the mouth). On average, EEG spikes preceded EMG bursts by 17.0 ± 3.7 ms and movement acceleration by 20.7 ± 2.5 ms (mean ± SD).

We next examined the temporal dynamics of tic-like movements during 40 min following injection. The number of tic events and EEG spikes peaked at 10–20 min, gradually declined after 25 min, and returned to baseline by 40 min (Figures 1F and 1G). The amplitude of EEG spikes remained relatively stable before progressively decreasing (Figure 1H). EMG amplitude and the speed of wrist and mouth movements, quantified in 10-min bins, robustly increased up

110 to 30 min post-injection before markedly attenuating (Figures 1I and S1F). The overall intensity
111 of tic-like movements, estimated from mean EMG amplitude and the area under the curve
112 (AUC) of wrist movement speed (10-min bins), peaked at 10 − 20 min and diminished
113 substantially by 30–40 min (Figures 1J, 1K, and S1G). Non-tic-associated EEG spikes became
114 more prominent after 35 min (Figures 1L and 1M). Thus, striatal disinhibition induced transient
115 tic-like movements lasting ~40 min in this model.
116
117 ***Tic-associated brain activation in motor and limbic structures***
118 To identify brain regions engaged during tic expression, we performed c-Fos
119 immunohistochemistry following unilateral striatal bicuculline injection (0.2 μg/μl, 0.20 μl; the
120 same dose as in the preceding experiments). Mice were perfused 90 min after injection, and
121 brain sections were processed for c-Fos staining (Figure 2A). c-Fos mapping revealed robust
122 neuronal activation in multiple brain structures ipsilateral to the injection site (Figures 2A-2C).
123 In the cortex, strong c-Fos expression was observed in medial prefrontal regions (including the
124 cingulate [Cg1], prelimbic [PrL], infralimbic [IL], and dorsal peduncular [DP] cortices), M1,
125 the secondary motor cortex (M2), and IC. Subcortical activation was evident in the BG,
126 including the dSTR, globus pallidus (GP), and subthalamic nucleus (STN). Thalamic activation
127 involved the motor thalamus (ventral anterior [VA] and ventrolateral [VL] nuclei), the sensory
128 thalamus (ventral posterolateral [VPL], ventral posteromedial [VPM], and posterior [Po]
129 nuclei), and the rostral intralaminar thalamic nuclei (rITN; central medial [CM], paracentral
130 [PC], and centrolateral [CL] nuclei). Beyond sensorimotor regions, limbic structures such as
131 the amygdala and hypothalamus also showed high levels of c-Fos expression. Thus, unilateral
132 striatal disinhibition elicited widespread activation across motor and limbic circuits, with strong
133 ipsilateral dominance (Figure 2D).

134

135 ***Insular cortical activity is associated with tic generation***

136 Given the widespread activation observed during tic generation, we next focused on IC,
137 since several studies have proposed it as a potential trigger site for tics and their preceding
138 "urges".[25,26] Consistent with this, human imaging studies have reported IC activation in TS
139 patients.[27,28]

140 To monitor tic-related activity in IC and M1 (the final cortical output node for motor
141 commands), we performed *in vivo* Ca^{2+} imaging using fiber photometry (Figures 3A and 3B).
142 Optical fibers were implanted into the ipsilateral M1 and bilateral IC one week after viral
143 injections of AAV1-Syn-GCaMP6f (Figure 3A). Following unilateral striatal disinhibition,
144 robust Ca^{2+} activity was observed in the ipsilateral M1 and IC, time-locked to motor tics
145 (Figures 3B and 3C). The contralateral IC also exhibited tic-associated activity. Analysis of
146 temporal dynamics revealed that tic-associated Ca^{2+} activity in the ipsilateral M1 and bilateral
147 IC peaked at 10–20 min post-injection and then gradually declined (Figures 3D and 3E),
148 paralleling the time course of tic-like movements and M1 EEG spikes (Figures 1F-1K, S1F, and
149 S1G).

150

151 ***The intralaminar thalamic nuclei relay basal ganglia outputs to the insular cortex***

152 We next investigated the neuronal pathway mediating IC activation following striatal
153 disinhibition. To identify outputs from the dSTR, we first injected AAV1-CAG-tdTomato into
154 the dSTR (Figure 4A). Anterogradely labeled axonal terminals were observed in the GP,
155 entopeduncular nucleus (EP), and substantia nigra pars reticulata (SNr), but not in IC or other
156 cortical regions.

157 To confirm the absence of a direct dSTR-IC projection, we injected AAV2retro-CAGGS-

158 EGFP into the middle part of IC along the rostrocaudal axis (Figure 4B). No retrogradely
159 labeled neurons were found in the striatum or in other BG nuclei (GP, EP, STN, and SNr).
160 Instead, labeled neurons were detected in the dorsomedial thalamus (dmTh), including the rITN,
161 the paraventricular/intermediodorsal nuclei (PV/IMD), and the mediodorsal nucleus (MD)
162 (Figure 4B and 4C). Notably, thalamic structures classically receiving BG outputs, such as the
163 motor thalamus (VA, VL, and ventromedial [VM] nucleus) and the parafascicular nucleus
164 (Pf),[29-31] contributed minimally to IC-projecting neurons.

165 Because the SNr is the largest BG output nucleus in rodents,[31] we hypothesized that SNr
166 neurons reach IC via the dmTh. A large proportion of SNr neurons are PV-positive and exhibit
167 projections similar to VGAT-positive neurons,[31,32] indicating that they are GABAergic
168 projection neurons. We injected AAV1-CAG-FLEX-tdTomato into SNr of PV-Cre mice (Figure
169 4D), revealing widespread projections to multiple thalamic regions, including the dmTh
170 (Figures 4D and S2).

171 To test whether dmTh-projecting SNr neurons connect with IC-projecting dmTh neurons,
172 we performed triple viral injections: 1) AAV2retro-CAGGS-Cre in the dmTh, 2) AAV1-CAG-
173 FLEX-tdTomato into SNr, and 3) AAV2retro-CAGGS-EGFP into IC (Figure 4E). SNr axon
174 terminals were closely apposed to IC-projecting dmTh neurons, particularly within the rITN.

175 These findings indicate that IC receives BG outputs via ITN, known targets of deep brain
176 stimulation (DBS) in TS patients.[33,34]

177

178 ***Chemogenetic inhibition of thalamo-insular pathway alleviates tic-like movements***

179 To determine whether the thalamo-insular pathway contributes to motor tic generation,
180 we tested its role using designer receptors exclusively activated by designer drugs (DREADD).
181 We then examined whether tic-like movements induced by striatal disinhibition were attenuated.

182 As an initial step, we examined whether direct inhibition of IC reduced tic expression.
183 AAV8-hSyn-hM4Di-mCherry was bilaterally injected into three rostrocaudally distinct IC sites
184 (Figures 5A and 5C). Thirty minutes after intraperitoneal administration of either vehicle or
185 clozapine-N-oxide (CNO; DREADD agonist), bicuculline was injected into the same dSTR site
186 via a guide cannula across three test sessions. To control for repeated injection effects, the
187 sequence was vehicle (1st test), CNO (2nd test), and vehicle (3rd test) (Figure 5E). Tic severity
188 was quantified during the 30-min period following bicuculline injection, when tics were
189 prominent, by measuring both the number of tics and the intensity of tic-associated body
190 movements, defined by movement speed (see STAR Methods). Chemogenetic inhibition of
191 bilateral IC significantly reduced both tic frequency and intensity (Figures 5F and 5G; Video
192 S2).

193 We next investigated whether chemogenetic inhibition of the dmTh-IC pathway affected
194 tic generation. To address this issue, AAV2retro-CAGGS-Cre was injected into bilateral IC and
195 AAV-DJ-EF1α-DIO-hM4Di-mCherry into bilateral dmTh (Figures 5B and 5D). Bilateral
196 inhibition of this pathway significantly reduced tic intensity, while tic frequency was unchanged
197 (Figures 5H and 5I; Video S2).

198 Because we used a relatively high dose of CNO (10 mg/kg) and CNO has been reported
199 to influence glutamatergic and dopaminergic systems,[35,36] we conducted control experiments
200 using mCherry-expressing viruses instead of hM4Di-mCherry (Figures 5A and 5B). CNO
201 administration in these controls had no significant effect (Figures 5J-5M).

202 Taken together, these results indicate that the thalamo-insular pathway contributes to tic
203 generation.

204

205 ***Chemogenetic inhibition of the thalamo-insular pathway alters downstream tic-associated***

206 ***cortical activity***

207 We next examined whether chemogenetic manipulation of the thalamo-insular pathway
208 altered activity in downstream cortical regions. Fiber photometry Ca^{2+} recordings were
209 performed in the ipsilateral M1 and bilateral IC of mice in which IC-projecting dmTh neurons
210 expressed inhibitory DREADD, using the same experimental timeline as in the preceding
211 experiment (Figure 6A). CNO administration reduced tic intensity without affecting tic
212 frequency, consistent with behavioral data (Figures 5H, 5I, and S3). During the CNO session,
213 tic-associated Ca^{2+} activity persisted (Figures 6B and 6C), but its amplitude was significantly
214 reduced in the ipsilateral M1 and ipsilateral IC (Figures 6C and 6D). In contrast, the amplitude
215 in the contralateral IC remained unchanged.

216 To further assess whether chemogenetic manipulation of IC or the dmTh-IC pathway
217 modulates tic-associated M1 activity at the single-cell level, we performed two-photon Ca^{2+}
218 imaging of GCaMP6f-expressing ipsilateral M1 neurons (Figures S4A and S4B). Following
219 bicuculline injection, M1 neurons exhibited temporally synchronized Ca^{2+} signals (Figures S4B
220 and S4C; see also Video S3). IC inhibition reduced Ca^{2+} event amplitudes in both superficial
221 (layer 2/3) and deep (layer 5/6) layers, whereas dmTh-IC pathway inhibition selectively
222 reduced amplitudes in the superficial layer. Event frequency in the superficial layer was
223 unaffected by either manipulation, whereas IC inhibition increased frequency in the deep layer.
224 For response probability of M1 Ca^{2+} signals to tic onsets (see STAR Methods), decreases were
225 observed in the superficial layer under both manipulations, whereas dmTh–IC pathway
226 inhibition uniquely led to an increase in the deep layer (Figures S4D-I).

227 These results indicate that inhibition of IC neurons or IC-projecting dmTh neurons
228 modulates M1 activity in a layer-specific manner, contributing to tic suppression.

229

DISCUSSION

We found that a striatal disinhibition-induced mouse model of tics exhibited brain activation across motor and limbic structures, including IC. We further provided anatomical evidence that BG outputs originating from the striatal motor domain are relayed to IC via ITN, which are known targets of DBS in intractable TS.[33,34] Finally, we demonstrated that chemogenetic inhibition of the thalamo-insular pathway suppressed tic symptoms. Collectively, these findings reveal an unexpected crosstalk between motor and limbic domains within the CBGTC network and suggest that aberrant activity in the thalamo-insular pathway contributes to the emergence of tics.

Animal model of tic disorders based on striatal disinhibition

Motor and vocal tics accompanied by premonitory urges are hallmark symptoms of TS patients. These individuals frequently manifest comorbid psychiatric and behavioral disorders, including OCD, ADHD, autism spectrum disorder (ASD), anxiety, depression, and sleep disorders.[7,8] Although recent genome-wide association studies (GWAS) and whole-exome sequencing studies have suggested some candidate genes contributing to TS pathophysiology, critical genes have not yet been identified.[37-39] Moreover, knockout mouse models of these candidate genes generally do not exhibit motor tics, or, if they do, the frequency is very low. Instead, some of these models display stereotyped behaviors such as excessive grooming or rearing, which more closely resemble OCD-like behaviors.[40,41] In contrast, postmortem studies in TS patients have revealed a reduction of striatal GABAergic interneurons.[21,22] Consistent with these findings, nonhuman primate models of motor and vocal tics induced by blocking GABAergic inputs have been well established (see also Figures 1 and S1 in our study).[15-19,42]

254 In addition to striatal interneurons, the striatum is also known to receive substantial GABAergic
255 inputs from "arkypallidal" neurons in GP (corresponding to the external globus pallidus [GPe]
256 in primates; see also Figure S1A).[43] Indeed, injections of a $GABA_A$ receptor antagonist into
257 primate GPe induce choreic dyskinesias.[44-46] Thus, dysfunction of the striato-GP network
258 through disruption of GABAergic tone may generate synchronized activity in BG output
259 neurons and subsequently M1 neurons, ultimately leading to involuntary movements.[42,47,48]
260

261 ***The insula is a key site responsible for tic generation***

262 Our study demonstrated that IC is robustly activated in a mouse model of tics induced by
263 striatal disinhibition (Figure 2). Tic-associated activity was observed in IC as well as in M1
264 (Figures 3, 6, and S4). Importantly, chemogenetic inhibition of IC alleviated tic-like behaviors
265 (Figure 5). These findings strongly suggest that IC serves as a key site responsible for tic
266 generation. Supporting this notion, human imaging studies in TS patients have demonstrated
267 IC activation.[27,28]

268 Intriguingly, we previously reported that the use of an oral splint, typically applied in the
269 treatment of temporomandibular disorders, produced immediate and marked therapeutic effects
270 on both motor and vocal tics in approximately two-thirds of TS patients.[49] Motivated by this
271 clinical observation, we sought to anatomically trace the ascending pathway of orofacial
272 proprioception in rodents, given that oral devices activate muscle spindles of the masseter. We
273 found that orofacial proprioceptive inputs are ultimately transmitted not to the primary sensory
274 cortex but rather to IC, via the supratrigeminal nucleus (Su5) and the caudo-ventromedial
275 subdivision of VPM (VPMcvm).[50,51] Taken together, these anatomical and clinical findings
276 suggest that oral splint insertion may modulate aberrant IC activity underlying tic generation in
277 TS patients.

278 IC is well known as a center of emotional processing and interoceptive awareness,
279 integrating signals generated by physiological body states.[52-54] In this context, abnormal IC
280 activity in TS patients may contribute not only to motor symptoms such as tics but also to
281 premonitory urges and comorbid psychiatric disorders, including OCD, ADHD, and ASD.
282
283 ***Why the intralaminar thalamic nuclei can be surgical targets in TS patients***
284 Historically, ablative procedures such as thalamotomy, pallidotomy, and subthalamotomy
285 were pioneering neurosurgical treatments for movement disorders.[55-57] Since the development
286 of DBS at the end of the last century, DBS targeting the internal globus pallidus (GPi) or STN
287 has become the gold standard for intractable Parkinson's disease and dystonia.[58-60] In contrast,
288 ITN have been empirically identified as effective DBS targets in TS patients.[61,62] However, the
289 mechanistic basis for this efficacy has remained unclear.
290 Anatomically, our study identified the dmTh, particularly the rITN, as a candidate relay
291 region of BG outputs to IC (Figure 4). Chemogenetic inhibition of IC-projecting dmTh neurons
292 attenuated tic-associated activity in IC (Figure 6). Moreover, this manipulation also suppressed
293 tic-related activity in M1 and reduced tic-like movements (Figures 5, 6, S3, and S4). These
294 results suggest that the dmTh-IC pathway transmits abnormal BG activity to IC, thereby
295 contributing to the exacerbation of motor tics.
296 Importantly, the caudal ITN (cITN), a clinical DBS target in TS patients, maintains
297 topographically organized connections with the CBGTC circuits (particularly the striatum and
298 cortex).[30,63] In contrast, the rITN exhibits widespread or loosely topographical projections to
299 multiple structures within these circuits.[64] Given that the rITN and the cITN are spatially
300 adjacent, the current spread from a DBS electrode implanted in the cITN may also influence
301 the rITN, thereby exerting therapeutic effects in TS patients. A future double-blinded clinical

302 trial directly comparing the rITN versus cITN stimulation will be warranted to determine the
303 optimal surgical target.
304
305 ***Crosstalk in motor and limbic networks in the cortico-basal ganglia-thalamo-cortical circuits***
306 The existence of crosstalk between motor and limbic networks within the CBGTC
307 circuits has long been debated. These circuits have traditionally been conceived as functionally
308 segregated, closed parallel loops, comprising motor, associative, and limbic loops that originate
309 from distinct cortical regions.[65,66] Consistent with this view, pharmacological manipulations in
310 the motor, associative, and limbic domains of the striatum or GPe selectively induce motor,
311 cognitive, and emotional disturbances, respectively.[19,45,67] Although IC is not included in the
312 classical definitions of the limbic system proposed by Papez,[68] converging evidence places IC
313 within a broader limbic network that links emotion, interoception, and behavior.[52,69] Importantly,
314 IC directly projects to the ventral striatum (striatal limbic domain).[70,71]
315 Our findings challenge this closed-loop model. In addition to the previously described
316 "limbic-to-motor" open loop (striatal limbic domain-SNr-motor thalamus-motor cortices
317 pathway),[32] we identified a complementary "motor-to-limbic" open loop (striatal motor
318 domain-SNr-dmTh-IC pathway; see also Figure S5). These subcortical interactions indicate that
319 motor and limbic domains within the CBGTC circuits are not strictly segregated, but instead
320 communicate bidirectionally. While the closed "motor cortices-BG motor domain-motor
321 thalamus-motor cortices" loop may account for the pathophysiology of simple motor tics, our
322 new framework more effectively explains the broad spectrum of symptoms observed in TS
323 patients, including motor and vocal tics, premonitory urges, and psychiatric comorbidities such
324 as OCD and ADHD. Dysfunction in the "motor-to-limbic" pathway may permit abnormal
325 motor signals to spread into limbic regions, leading to emotional and cognitive symptoms. In

this context, targeted intervention of aberrant neuronal processing in the "motor-to-limbic" circuit (i.e., the dmTh-IC pathway) could be therapeutically beneficial. Approaches such as ultrasound neuromodulation or thermoablation, which can access deep brain structures, may provide therapeutic benefits in TS patients. In contrast, interventions such as transcranial direct current or transcranial magnetic stimulation, when applied to M1, may inadvertently disrupt voluntary motor control.[72-74]

Beyond subcortical interactions, motor-limbic crosstalk may also occur at the cortical level. The limbic cortex (e.g., IC) has limited direct connections to M1,[71] but aberrant IC activity may influence motor outputs indirectly through other cortical structures, such as the sensory cortex, or through subcortical feedback loops.[32] Thus, motor and limbic loops communicate at both subcortical and cortical levels, and abnormal dynamics across these multiple pathways may underlie the recurrent and dynamic nature of tic generation.

In conclusion, our study suggests that normalization of IC activity could restore balance between motor and limbic circuits and improve both motor and emotional symptoms in TS.

RESOURCE AVAILABILITY

Lead contact

Further information and requests for resources and reagents should be directed to the lead contact, Yoshihisa Tachibana (yoshi@med.kobe-u.ac.jp).

Materials availability

The study did not produce new unique reagents.

Data and code availability

Tic-associated raw data have been deposited at Mendeley Data. Accession numbers are listed in the key resources table. This paper does not report original code. Any additional information required to reanalyze the data reported in this paper is available from the lead contact upon request.

ACKNOWLEDGMENTS

We thank A. Nambu, S. Yamamoto, K. Toda, T. Hirata, K. Tamada, N. Nakai, and Y. Shintani for their valuable comments and discussions. We are grateful to H. Shima and M. Shiramizu for technical assistance with animal care. This work was supported by the Japan Society for the Promotion of Science (JSPS) KAKENHI (18K06852, 22K19732, 24H00422, and 24K02339 to Y.T.; 24H00620 to T.T.), by the Taiju Life Social Welfare Foundation (to Y.T.), and by AMED under Grant Number JP23wm0625001 (to K.K.).

AUTHOR CONTRIBUTIONS

H.K. and Y.T. conceived the study and designed the experiments. H.K. performed the majority of the experiments, and N.T. conducted some of the histological experiments. H.K. analyzed the data. K.K. provided materials. H.K. and Y.T. wrote the manuscript with editorial input from T.T.

DECLARATION OF INTERESTS

The authors declare no competing interests.

375 **EXPERIMENTAL MODEL AND SUBJECT DETAILS**

376

377 ***Animals***

378 All animal procedures were approved by the Institutional Animal Care and Use
379 Committees of Kobe University. Male C57BL/6J (6−16 weeks old) and male PV-Cre mice[75]
380 (6–10 weeks old) were used. All animals were maintained in the animal facility at Kobe
381 University. Animals were group-housed under controlled temperature (23−25℃) in a 12/12 h
382 light-dark cycle (lights on from 6 AM to 6 PM) with free access to food and water. Animals
383 implanted with a guide cannula or optical fibers were single-housed after surgery to prevent
384 damage to the implanted devices.

385

386 **METHOD DETAILS**

387

388 ***Head plate attachment***

389 The first surgery was performed on mice aged 6−10 weeks. Mice were anesthetized with
390 ketamine (80 mg/kg, intraperitoneally [i.p.]; Ketalar, Daiichi Sankyo, Tokyo, Japan) and
391 xylazine (12 mg/kg, i.p.; Seractar, Elanco Japan, Tokyo, Japan), and mounted on a stereotaxic
392 apparatus (SR-6M-HT, Narishige, Tokyo, Japan). To prevent corneal drying, gentamicin eye
393 ointment (TAKATA Pharmaceutical Co., Saitama, Japan) was applied to both eyes. After
394 subcutaneous injection of epinephrine-containing lidocaine (Xylocaine DENTAL, Dentsply
395 Sirona, York, PA, USA), the scalp was incised to expose the skull. Except for anatomical
396 neuronal tracing experiments, a custom-made metal head plate was affixed to the skull with
397 dental cement (G-CEM ONE neo, GC.dental, Tokyo, Japan) to secure the animal in a custom-

398 built fixation apparatus.

399

400 ***Viral injection***

401 For viral delivery, a small craniotomy was performed on the same day as head plate
402 attachment. A small burr hole was made using a dental drill (MICROMOTOR LM-III,
403 GC.dental), with supplementary ketamine/xylazine administered as needed. Viral solutions
404 were pressure-injected through a glass micropipette attached to a microinjector (I-31, Narishige,
405 Tokyo, Japan). The micropipette was left in place for at least 5 min to minimize backflow and
406 prevent viral spread to adjacent brain regions. All stereotaxic coordinates were determined
407 according to the Paxinos Mouse Brain Atlas (third edition).[76]

408 For viral tracing experiments, AAV1-CAG-tdTomato (2.0×10^{13} vector genomes [vg]/ml,
409 diluted 1:2 in saline) or AAV1-CAG-Flex-tdTomato (1.6×10^{13} vg/ml, diluted 1:2 in saline) was
410 injected unilaterally into the dorsal striatum (dSTR; 0.10–0.15 µl/injection, AP: 0.0 mm, ML:
411 2.7 mm, DV: –3.5 mm from the bregma) or the substantia nigra pars reticulata (SNr; 0.10–0.15
412 µl/injection, AP: –3.1 mm, ML: 1.65 mm, DV: –4.6 mm). AAV2retro-CAGGS-EGFP ($6.8 \times$
413 10^{12} vg/ml, diluted 1:2 in saline) or a mixture of AAV2retro-CAGGS-EGFP and AAV1-CAG-
414 tdTomato (diluted 1:1:1 in saline; red fluorescence data not shown) was injected into the middle
415 portion of the insular cortex (IC) along the rostrocaudal axis (0.10–0.15 µl/injection; AP: 0.5
416 mm, ML: 3.3 mm, DV: –3.6 mm). For labeling dorsomedial thalamus (dmTh)-projecting
417 neurons in other brain regions, AAV2retro-CAGGS-Cre (7.3×10^{12} vg/ml, diluted 1:2 in saline)
418 was injected into the dmTh (0.20 µl/injection, AP –1.5 mm, ML: 0.5 mm, DV: –3.5 mm).

419 For experiments targeting IC neurons with hM4Di-mCherry or mCherry using the
420 designer receptors exclusively activated by designer drugs (DREADD) system, AAV8-hSyn-

421 hM4Di-mCherry (2.2 × 10^{13} vg/ml, diluted 1:2 in saline) or AAV8-hSyn-mCherry (2.1 × 10^{13}
422 vg/ml, diluted 1:2 in saline) was injected bilaterally into three rostrocaudally distinct IC sites:
423 anterior IC (aIC; 0.20 µl/injection, AP: 1.5 mm, ML: ±2.7 mm, DV: –3.2 mm), middle IC (mIC;
424 0.30 µl/injection, AP: 0.5 mm, ML: ±3.3 mm, DV: –3.6 mm), and posterior IC (pIC; 0.20
425 µl/injection, AP: –0.5 mm, ML: ±3.7 mm, DV: –3.5 mm).

426 For experiments targeting IC-projecting dmTh neurons with hM4Di-mCherry or mCherry,
427 AAV2retro-CAGGS-Cre (7.3 × 10^{12} vg/ml, diluted 1:2 in saline) was injected bilaterally into
428 three distinct IC sites (aIC, mIC, and pIC; same coordinates as above), and AAV-DJ-EF1α-DIO-
429 hM4Di-mCherry (1.5 × 10^{13} vg/ml, diluted 1:2 in saline) or AAV-DJ-EF1α-DIO-mCherry (2.0
430 × 10^{13} vg/ml, diluted 1:2 in saline) was injected bilaterally into the dmTh (0.40 µl/injection, AP:
431 –1.5 mm, ML: ±0.5 mm, DV: –3.5 mm).

432 For fiber photometry, AAV1-Syn-GCaMP6f-WPRE-SV40 (2.0 × 10^{13} vg/ml, diluted 1:2
433 in saline) was injected unilaterally into the primary motor cortex (M1; 0.20 µl/injection, AP:
434 0.5 mm, ML: 1.0 mm, DV: –1.3 mm) or bilaterally into the mIC (0.20 µl/injection, AP: 0.5 mm,
435 ML: 3.3 mm, DV: –3.6 mm). One week later, optical fibers (1.25 mm ferrule OD, 400 µm core,
436 NA 0.5; cat# R-FOC-BL400C-50NA, RWD Life Science, Guangdong, China) were implanted
437 200 µm above the injection sites (M1 or mIC) under isoflurane anesthesia (1.0%; Viatris,
438 Pittsburgh, PA, USA) and fixed with dental resin (UNIFAST II, GC.dental).

439 For two-photon microscopic imaging, a circular craniotomy (2.5 mm in diameter) was
440 made over M1 (center, AP: 0.5 mm, ML: 1.0 mm) ipsilateral to the striatal bicuculline injection
441 (see below) under isoflurane anesthesia, 1-2 days after the head plate attachment. After the
442 craniotomy, AAV1-Syn-GCaMP6f-WPRE-SV40 (2.0 × 10^{13} vg/ml, diluted 1:2 in saline) was
443 injected into two depths of the ipsilateral M1 (300 µm and 500 µm below the brain surface,
444 0.20 µl at each site). The cortical surface was covered with a glass window composed of two

445 coverslips (2 and 4.5 mm in diameter, respectively; Matsunami Glass, Osaka, Japan), using
446 transparent adhesive (NOR-61, Norland Products, Jamesburg, NJ, USA). The edges of the glass
447 window were sealed with dental cement (Fuji Lute, GC.dental) and adhesive resin cement
448 (Super Bond, Sun Medical, Shiga, Japan).
449
450 ***EEG and EMG electrode implantation***
451 In the experiments shown in Figures 1 and S1, electroencephalogram (EEG) and
452 electromyogram (EMG) electrodes were implanted under ketamine/xylazine anesthesia on the
453 same day as head plate attachment. In the experiment shown in Figure 5, EEG electrodes were
454 implanted under isoflurane anesthesia, three weeks after viral injections.
455 For EEG electrode implantation, small burr holes were made above the ipsilateral M1
456 (AP: 0.5 mm, ML: 1.0 mm) and the contralateral visual cortex (AP: –3.5 mm, ML: 3.0 mm;
457 reference electrode). Metal screws serving as electrodes were implanted into the holes and
458 secured to the skull with dental cement (G-CEM ONE neo, GC.dental). Screws were connected
459 to terminal connectors via copper wires, and the connectors were mounted on the head plate
460 using dental resin (UNIFAST II, GC.dental).
461 For EMG electrode implantation, mice received a subcutaneous injection of epinephrine-
462 containing lidocaine in the contralateral upper arm. The skin was incised to expose the triceps
463 muscle, and two PFA-coated stainless-steel wires (7-strand, 0.0055” in diameter; cat# 793200,
464 A-M Systems, Sequim, WA, USA) were inserted into the muscle and secured with tissue
465 adhesive (Vetbond, 3M Co., Ltd, St. Paul, MN, USA) and suture thread. The implanted wires
466 were connected to terminal connectors as described above.
467
468 ***Guide cannula implantation***

469 When repeated bicuculline injections were required for DREADD experiments (see
470 below for details), a guide cannula was chronically implanted into the unilateral dSTR to
471 minimize variability in behavioral outcomes caused by differences in bicuculline injection sites.
472 After a craniotomy under isoflurane anesthesia, a 5-mm-long guide cannula (AG-5T, Eicom,
473 Kyoto, Japan) was implanted vertically into the dSTR (AP: 0.0 mm, ML: 2.7 mm, DV: –3.5
474 mm) for DREADD experiments not involving neuronal recording. For DREADD experiments
475 combined with fiber photometry or two-photon calcium imaging, an 8-mm-long guide cannula
476 (CXG-8T, Eicom) was implanted sagittally from caudal to rostral at a 40° angle to avoid
477 interference with the optical fibers or cranial window. The guide cannula was then anchored to
478 the skull with dental cement (G-CEM ONE neo, GC.dental).
479
480 ***Striatal local bicuculline injection***
481 Bicuculline methochloride (cat# B7686, Sigma, St. Louis, MO, USA) was dissolved in
482 saline at 100 mg/ml to prepare stock aliquots, which were stored at −30°C. Immediately before
483 each injection, the stock solution was diluted in saline to a final concentration of 0.2 mg/ml.
484 For single-injection experiments, a small burr hole was made under isoflurane anesthesia,
485 which was discontinued immediately afterward. A disposable glass micropipette filled with
486 bicuculline solution was gently inserted into the dSTR (AP: 0.0 mm, ML: 2.7 mm, DV: –3.5
487 mm). After recording baseline behavioral data, bicuculline was injected using a glass
488 micropipette attached to a microinjector (I-31, Narishige). The micropipette was left in place
489 until the end of the experiment to minimize tissue damage and prevent leakage into adjacent
490 brain regions.
491 For repeated-injection experiments (e.g., in DREADD experiments), an injection cannula
492 (AMI-5T or CXMI-8T, Eicom) attached to a microsyringe (cat# N1701, Hamilton, Reno, NV,

493 USA) containing bicuculline solution was inserted into the chronically implanted guide cannula
494 (see above).
495 In both injection protocols, 0.20 µl of bicuculline was injected over ~1 min.
496
497 ***Chemogenetic manipulation***
498 To chemogenetically suppress the activity of specific neurons, the DREADD
499 agonist clozapine-N-oxide (CNO; cat# HY-17366, MedChemExpress, Monmouth Junction,
500 NJ, USA) was administered i.p. to mice expressing hM4Di-mCherry or mCherry (control) in
501 IC neurons or IC-projecting dmTh neurons. CNO was dissolved in dimethyl sulfoxide
502 (DMSO; cat# 13445-74, Nacalai Tesque, Kyoto, Japan) at 100 mg/ml to prepare stock aliquots,
503 which were stored at −30℃. The stock solution was diluted in saline to a final concentration
504 of 2 mg/ml immediately before use.
505 In the experiments shown in Figures 5, 6, S3, and S4, CNO or vehicle (2% DMSO) was
506 administered at 5 ml/kg i.p (equivalent to 10 mg/kg CNO) 30 min before baseline recordings.
507 Each trial was conducted with an interval of at least 72 h to avoid residual effects of CNO or
508 bicuculline from the previous session.
509
510 ***EEG and EMG recordings***
511 After the mice were secured in the head-fixation apparatus, EEG and EMG electrodes
512 were connected to an amplifier with an integrated A/D converter (PowerLab 26T,
513 ADInstruments, Dunedin, New Zealand). EEG and EMG signals were sampled at a sampling
514 rate of 10 kHz. Behavioral videos were simultaneously recorded at 100 frames/s with a digital
515 camera (acA800-510um, Basler, Ahrensburg, Germany) positioned in front of the mice.
516 Baseline recordings were obtained for 5 min before bicuculline injection. Following

517 bicuculline injection, recordings continued for 40 min. The acquired EEG and EMG data were
518 preprocessed in MATLAB (MathWorks, Natick, MA, USA). After downsampling to 1 kHz, the
519 data were bandpass filtered (EEG: 0.5 – 120 Hz; EMG: 5 – 500 Hz) and notch-filtered at 60 Hz
520 to remove line noise.
521
522 ***Fiber photometry recording***
523 The implanted optical fibers in the ipsilateral M1 or bilateral IC of mice expressing
524 GCaMP6f in these brain regions were connected to a multichannel fiber photometry system
525 (R821, RWD Life Science, Shenzhen, China) via a bundle branching patch cord (BBP(4)
526 400/430/1100-0.57_2m_FCM-4xZF1.25(F)_LAF, Doric Lenses, Québec, Canada), which
527 enabled simultaneous recording from multiple brain regions. Dual-wavelength recording (470
528 nm and 410 nm) was performed: the 470-nm LED excitation light was used to detect GCaMP6f
529 fluorescence, whereas the 410-nm one was used to measure calcium-independent isosbestic
530 signals. Neuronal Ca^{2+} signals and behavioral videos were synchronously recorded at 60 Hz.
531 Recordings were conducted for 5 min before and 40 min after bicuculline injection.
532 Data were analyzed using custom-written MATLAB scripts. Briefly, both 470-nm and
533 410-nm signals were smoothed using a locally weighted linear regression filter to reduce high-
534 frequency noise. The fitted control signal was obtained by regressing the 410-nm signal against
535 the 470-nm signal using a quantile regression method. $\Delta F/F$ was calculated as $(F-F_0)/F_0$, where
536 F represents the 470-nm signal and F_0 represents the fitted control signal.
537
538 ***In vivo two-photon microscopic calcium imaging***
539 Two-photon images were acquired from the mice expressing GCaMP6f in the ipsilateral
540 M1 using an $A1MP^+$ system (NIS-Elements, Nikon Instech Co., Ltd, Tokyo, Japan) equipped

541 with a 10× water-immersion objective lens (numerical aperture [NA], 0.3; working distance 3.5
542 mm; cat# MRH07120, Nikon Instech Co., Ltd) and a mode-locked Ti:sapphire Chameleon Ultra
543 II laser (Chameleon Vision, Coherent, Santa Clara, CA, USA) set at 950 nm.[77] To quantify
544 neuronal activity, time-lapse images were acquired at a resolution of 512 × 512 pixels (scanning
545 rate, 2 Hz; 2× digital zoom).

546 Before bicuculline injection, two continuous image series of 1000 frames each were
547 acquired from the ipsilateral M1 at depths of 250 and 500 μm from the cortical surface. After
548 bicuculline injection, continuous 1000-frame images were captured again from the same fields
549 of view. Images were repeatedly acquired for 5-25 min after bicuculline injection. As shown in
550 Figures 1 and S1, this period corresponds to the time window in which tic-like movements were
551 clearly observed.

552 During two-photon microscopic imaging, behavioral videos were simultaneously
553 recorded at 30 frames/s with an analog infrared-sensitive CCD camera (ITC-405HIR, ITS,
554 Tokyo, Japan).

555

556 ***Histology***

557 Mice were deeply anesthetized with ketamine/xylazine and transcardially perfused with
558 4% paraformaldehyde (PFA). The brain was extracted, post-fixed in 4% PFA overnight, and
559 soaked in 15% and then 30% sucrose for 2-3 days for cryoprotection. The brains were sectioned
560 into 50-μm coronal slices on a microtome (OFT5000, Bright Instruments, Cambridgeshire, UK).

561 For c-Fos immunohistochemistry, brain slices were permeabilized with 0.5% Triton X-
562 100 (Cat# 35501-15, Nacalai Tesque) in PBS for 3 h at room temperature. After blocking with
563 5% bovine serum albumin (BSA; Cat# 01860-36, Nacalai Tesque) for 1 h, the slices were
564 incubated overnight at 4℃ with primary antibody against c-Fos (cat# sc-52, Santa Cruz

565 Biotechnology, Dallas, TX, USA; 1:1000) diluted in PBS. After washing in PBS, the slices were
566 incubated overnight at 4°C with Cy3-conjugated anti-rabbit IgG secondary antibody (cat# 711-
567 165-152, Jackson ImmunoResearch, West Grove, PA; 1:1000) in PBS. The slices were then
568 mounted on glass slides with DAPI-containing mounting medium (H-1200, Vector Laboratories,
569 Newark, CA, USA).
570 Fluorescence images were captured using a KEYENCE BZ-X810 microscope
571 (KEYENCE, Osaka, Japan) with a 10× objective lens (NA 0.30) or an Olympus FV-3000
572 confocal microscope (Olympus, Tokyo, Japan) equipped with a 40× objective lens (NA 0.95).
573

574 **QUANTIFICATION AND STATISTICAL ANALYSIS**

575

576 ***Behavioral analysis***

577 Tic-like movements were quantified in head-fixed mice following unilateral striatal
578 bicuculline injection. User-defined body parts were tracked using DeepLabCut
579 (https://github.com/DeepLabCut).[78] A custom-made MATLAB script was used to compute the
580 speed (i.e., scalar velocity) and acceleration of movements in the contralateral wrist or the
581 contralateral corner of the mouth based on the DeepLabCut tracking trajectories. Motor tics
582 were detected based on the timing of spike signals in the ipsilateral M1 cortical activity
583 obtained from EEG or fiber photometry recordings (see below for details), because the M1
584 spikes were generally accompanied by motor tics (Figures 1, 3, and S1). For EEG-based tic
585 detection, the speed of body movements was calculated within a 0–0.3 s time window after
586 M1 spikes. For fiber photometry-based tic detection, the speed was calculated in a −0.2 to

587 +0.1 s window relative to the M1 spike, as tic-related Ca^{2+} activity typically lagged behind the
588 onset of tic-like movements by ~0.2 s (see Figure 3).
589 In Figures 1K and S1, the area under the curve (AUC) of movement speed of the
590 contralateral wrist and mouth was calculated within a 0–0.3 s time window after EEG spikes
591 associated with tics as follows:
592 $$\text{AUC} = \sum_{t=1}^{0.3\times Fs} St \times \frac{1}{Fs}$$
593 , where *St* is the speed of the targeted body part at each time point after an EEG spike, and Fs
594 is the sampling frequency of the behavioral video.
595 A movement was classified as a motor tic if the speed of the contralateral wrist or corner
596 of the mouth exceeded the mean + 0.5 SD and the maximum acceleration exceeded the mean
597 + 2 SD of the entire recording period. This automated detection method was largely consistent
598 with tic identification by visual inspection.
599 For DREADD experiments, tic intensity was calculated as ($S_{wrist}/S1_{wrist}$ +
600 $S_{mouth}/S1_{mouth}$)/2, where S is the average speed of the contralateral wrist or contralateral corner
601 of the mouth during tic expression (0-30 min after bicuculline injection) and S1 is that of the
602 first test (vehicle injection). The relative intensity value of the first test was therefore set to 1.
603 During *in vivo* two-photon imaging, the resolution of behavioral monitoring with an
604 analog infrared-sensitive CCD camera was insufficient for accurate tracking of mouth-corner
605 movements because of the low light intensity. Therefore, only forelimb trajectories were used
606 to assess tic-like movements. Forelimb tics were automatically detected when their speed
607 exceeded the mean + 0.5 SD and their peak acceleration exceeded the mean + 2 SD. Although
608 this method relied solely on forelimb speed, detected tic onsets were largely consistent with
609 those identified by an experienced observer.
610

611 ***Spike detection and signal analysis***

612 In the analyses of EEG and fiber photometry data, preprocessed signals (as described in
613 the "EEG and EMG recordings" and "Fiber photometry recording" sections) were converted
614 into robust *Z* scores. Because our data contained numerous spike signals (i.e., outliers), we
615 used a robust z score based on the median and interquartile range (IQR, representing the
616 central 50% of the distribution) to reduce the influence of outliers, in contrast to a
617 conventional mean- and SD-based *Z* score.[79]

618 The robust *Z* score was calculated as:

619 robust *Z* score = (x – median[x])/normalized IQR (NIQR)

620 , where NIQR was obtained by converting the IQR to the equivalent of 1 SD in a normal
621 distribution by multiplying by a normalization factor of 0.7413. If the data followed a normal
622 distribution, the robust *Z* score coincided with the conventional *Z* score.

623 Signal peaks with a prominence of at least 1 × NIQR were detected using the
624 "findpeaks" function in MATLAB. The prominence values of the detected peaks were then
625 subjected to k-means clustering to automatically determine the detection threshold. For EEG
626 data, the number of clusters was set to 3; for fiber photometry data, it was set to 4. Peaks
627 classified into the cluster with the lowest prominence were excluded as non-spike events, and
628 the remaining peaks were defined as spike signals.

629 For calculating the mean amplitude of tic-related Ca^{2+} spikes shown in Figures 3E and
630 6D, the average robust *Z* score of the prominence values was computed within a 0–0.3 s time
631 window following the onset of tic-like movements.

632

633 ***EMG analysis***

634 For quantification of EMG amplitude in Figure 1, we calculated an EMG envelope, a
635 smoothed curve that tracks temporal changes in EMG signal amplitude.[80] To compute the
636 envelope, the preprocessed signals (as described in the "EEG and EMG recordings" section)
637 were rectified and subsequently low-pass filtered at 2 Hz. The envelope values were then
638 normalized using the robust *Z* score, as described in the "Spike detection and signal analysis"
639 section. For the mean EMG amplitude shown in Figure 1J, the average robust Z score of
640 EMG amplitude was calculated within a 0–0.3 s window following EEG spikes associated
641 with tics.
642
643 ***Image analysis***
644 Images were analyzed using Fiji/ImageJ (National Institutes of Health, Bethesda, MD,
645 USA) and MATLAB.
646 For counting c-Fos positive cells in Figure 2, images were binarized using the built-in
647 auto-threshold "Triangle" function in ImageJ. After background noise was removed using the
648 "Remove Outliers" function, c-Fos positive cells were automatically counted using the
649 "Analyze Particles" function.
650 For counting EGFP-labeled thalamic neurons in Figure 4, coronal sections containing
651 target brain regions were selected at 300-μm intervals, and EGFP-positive cells were
652 manually counted. Cell counts from all sections in each thalamic region were summed and
653 normalized to those in the ventromedial (VM) thalamus.
654 For quantification of tdTomato-labeled axonal projections originating from the
655 substantia nigra pars reticulata (SNr) in Figure S2, images were binarized using the built-in
656 auto-threshold "Triangle" function in ImageJ to separate axonal fluorescence from

657 background. The fraction of suprathreshold pixels was calculated for each thalamic subregion
658 and normalized to the value in VM thalamus.

659 Two-photon Ca^{2+} images were corrected for focal plane displacement using the
660 "TurboReg" plug-in in ImageJ. To estimate neuronal activity, regions of interest (ROIs) were
661 determined using a semi-automated MATLAB-based toolbox with a graphical user interface
662 (EZcalcium; https://github.com/porteralab/EZcalcium).[81] A Ca^{2+} event was defined as a
663 fluorescence increase with a peak amplitude exceeding the baseline + 2 SD, where baseline
664 was defined as the 35th percentile of the total fluorescence distribution.[82] The mean amplitude
665 and frequency of Ca^{2+} events were calculated for each detected neuron.

666 To assess response probability, we quantified how reliably each neuron responded to tic-
667 like movements. A neuron was considered "responsive" if the fluorescence intensity in the
668 two frames after tic onset exceeded the mean of the two preceding frames by more than 2 SD.
669 Response probability was calculated by dividing the number of responsive events by the total
670 number of tic events.

671

672 ***Statistics***

673 Statistical analyses were performed using MATLAB and R (version 4.4.2; with the
674 "tidyverse", "rstatix", "afex", "emmeans" packages). Details of statistical tests are provided in
675 the figure legends. Statistical tests included paired *t*-test, one-sample *t*-tests with Holm
676 correction, one-way ANOVA (independent or repeated-measures) followed by pairwise *t*-tests
677 with Holm correction, and Kruskal-Wallis test followed by Dunn's multiple comparison tests
678 with Holm correction.

679 We did not routinely perform formal tests for normality, as their results are highly
680 sensitive to sample size. When the sample size was large ($n > 30$), *t*-tests are generally robust

to moderate deviations from normality. In such cases, we visually inspected the data distribution and applied parametric tests unless the data exhibited extreme skewness or kurtosis. When the sample size was small, we considered reliable estimation of the population distribution difficult, and we generally used parametric tests unless there was a clear reason to assume non-normality.

Data analyzed with parametric tests are presented as mean ± SEM, while those analyzed with non-parametric tests are shown as box plots. Box plots indicate the 25th and 75th percentiles, the median, and whiskers extending to data within a 1.5 x IQR. All tests were two-tailed with significance set at $\alpha = 0.05$.

691 **FIGURE LEGEND**

692

693 **Figure 1. Striatal disinhibition induces tic-like movements and tic-related EEG spikes in**
694 **the ipsilateral primary motor cortex (M1).**

695 (A) Schematic of electrophysiological recordings in the unilateral striatal bicuculline-induced
696 tic mouse model.

697 (B) Coronal brain section showing the injection site in the dorsal striatum (dSTR; arrow). Scale
698 bar, 500 μm.

699 (C and D) Representative traces of electroencephalogram (EEG) from the ipsilateral M1 (gray),
700 electromyogram (EMG) from the contralateral triceps muscle (red), and wrist movement speed
701 of the contralateral forelimb (blue) following bicuculline injection. Black arrows indicate tic-
702 like movement onsets. The region outlined by the red dashed rectangle in (C) is shown at higher
703 magnification in (D).

704 (E) Averaged traces of EMG from the contralateral triceps muscle (pink) and wrist movement
705 speed (blue), aligned to the onsets of EEG spikes recorded in the ipsilateral M1 during the 40-
706 min period following bicuculline injection (n = 9 mice). The black arrow indicates the mean
707 latency of tic onsets relative to EEG spike onsets. Shaded areas represent mean ± SEM.

708 (F-H) Time course of tic counts (F), frequency (G) and mean amplitude (H) of EEG spikes
709 recorded in the ipsilateral M1, plotted in 5-min bins after bicuculline injection (n = 9 mice).

710 (I) Averaged traces of EMG from the contralateral triceps muscle (pink) and wrist movement
711 speed (blue), aligned to the onsets of EEG spikes recorded in the ipsilateral M1, plotted
712 separately for successive 10-min epochs following bicuculline injection (n = 9 mice). Data are
713 presented in the same format as in (E).

714 (J and K) Time course of mean EMG amplitude (J) and the area under the curve (AUC) of the

715 contralateral wrist movement speed (K) within a 0–0.3 s time window following EEG spikes
716 associated with tics, plotted in 10-min bins after bicuculline injection (n = 9 mice).
717 (L) Representative traces showing EEG spikes in the ipsilateral M1 not accompanied by tic-
718 like movements (black arrows).
719 (M) Time course of the percentage of EEG spikes accompanied by tic-like movements, plotted
720 in 10-min bins after bicuculline injection (n = 9 mice).
721 For (H) and (M), if no EEG spikes occurred in a given time bin, the value for that bin was set
722 to 0 for individual data points; however, these bins were excluded from group means and SEMs.
723 Data are presented as mean ± SEM; individual mouse data are shown in gray.
724 See also Figure S1 and Video S1.
725
726 **Figure 2. Tic-associated brain activation revealed by c-Fos immunohistochemistry**
727 (A) Experimental timeline. Ninety minutes after unilateral bicuculline injection into the dSTR,
728 mice were perfused, paraformaldehyde-fixed, and brain sections were processed for c-Fos
729 immunohistochemistry. Top right, representative coronal section showing the striatal injection
730 site (arrow) stained for c-Fos. Scale bar, 500 μm.
731 (B) Representative images of c-Fos immunostaining in the contralateral and ipsilateral dSTR at
732 the anteroposterior (AP) level of +0.26 mm from the bregma. Scale bar, 500 μm.
733 (C) Representative c-Fos immunostaining in selected brain regions across cortical, basal
734 ganglia, thalamic, and limbic structures. Coronal sections at the indicated AP levels are shown.
735 Scale bars, 500 μm.
736 (D) Quantification of c-Fos-positive cells in the contralateral (gray) and ipsilateral (pink)
737 hemispheres across brain regions. Data are presented as mean ± SEM; individual mouse data
738 are shown in gray (n = 8 mice). Statistical analyses were performed using paired *t*-tests (*p*-

739 values were not corrected for multiple comparisons). *p < 0.05; **p < 0.01; ***p < 0.001.
740 Abbreviations: Amyg, amygdala; Cg1, cingulate cortex area 1; cITN, caudal intralaminar
741 thalamic nuclei; CL, centrolateral thalamic nucleus; CM, central medial thalamic nucleus; DP,
742 dorsal peduncular cortex; GP, globus pallidus; IC, insular cortex; IL, infralimbic cortex; IMD,
743 intermediodorsal thalamic nucleus; M2, secondary motor cortex; MD, mediodorsal thalamic
744 nucleus; PC, paracentral thalamic nucleus; Pf, parafascicular thalamic nucleus; Pir, piriform
745 cortex; Po, posterior thalamic nuclear group; PrL, prelimbic cortex; PV, paraventricular
746 thalamic nucleus; rITN, rostral intralaminar thalamic nuclei; STN, subthalamic nucleus; VA,
747 ventral anterior thalamic nucleus; VL, ventrolateral thalamic nucleus; VM, ventromedial
748 thalamic nucleus; VPL, ventral posterolateral thalamic nucleus; VPM, ventral posteromedial
749 thalamic nucleus.
750
751 **Figure 3. Insular cortical activity is associated with tic generation**
752 (A) Schematic of fiber photometry recordings (top). AAV1-Syn-GCaMP6f was injected into
753 the ipsilateral M1 and bilateral IC. Representative coronal sections showing GCaMP6f-
754 expression and optic fiber placements (dashed lines) in M1 and IC (bottom). Scale bars, 500
755 μm.
756 (B) Representative traces of Ca^{2+} signals in the ipsilateral M1, ipsilateral IC, and contralateral
757 IC, together with wrist and mouth-corner movement speeds, following unilateral bicuculline
758 injection,
759 (C) Averaged Ca^{2+} signals in the ipsilateral M1, ipsilateral IC, and contralateral IC, aligned to
760 tic onsets during the 40-min post-injection period (n = 8 mice).
761 (D) Same data as in (C), plotted separately for successive 10-min epochs following bicuculline
762 injection. Shaded areas represent mean ± SEM.

763 (E) Time course of mean amplitudes of tic-related Ca^{2+} spikes in the ipsilateral M1, ipsilateral
764 IC, and contralateral IC, plotted in 10-min bins after bicuculline injection. Data are presented
765 as mean ± SEM; individual mouse data are shown in gray.
766
767 **Figure 4. The intralaminar thalamic nuclei relay basal ganglia output to the insular cortex**
768 (A) Anterograde tracing from the dSTR. Injection of AAV1-CAG-tdTomato into the
769 dSTR labeled axon terminals in GP, entopeduncular nucleus (EP), and substantia nigra pars
770 reticulata (SNr), but not in M1, M2, or IC. Scale bars, 500 μm.
771 (B) Retrograde tracing from IC. Injection of AAV2retro-CAGGS-EGFP into the middle IC
772 (along the rostrocaudal axis) labeled neurons in the dorsomedial thalamus (dmTh), including
773 the rITN, PV/intermediodorsal thalamic nuclei (IMD), and MD, but not in the striatum or other
774 basal ganglia nuclei (GP, EP, STN, and SNr). Minimal labeling was observed in the motor
775 thalamus (VM, and VA/VL) and Pf. tdTomato fluorescence in IC (labeled by AAV1-CAG-
776 tdTomato) is shown for reference as the injection site. Scale bars, 500 μm.
777 (C) Quantification of thalamic inputs to IC, expressed as the $\log_{10}$ ratio of labeled neurons
778 relative to the number of neurons in VM thalamus (n = 5 mice). Data are presented as mean
779 (black dots) ± SEM.
780 (D) Anterograde tracing from parvalbumin (PV)-positive neurons in SNr of PV-Cre mice.
781 Injection of AAV1-CAG-FLEX-tdTomato revealed widespread projections to multiple thalamic
782 regions, including the dmTh. Scale bars, 500 μm.
783 (E) Triple viral tracing strategy to assess connectivity between SNr and IC via the dmTh.
784 AAV2retro-CAGGS-Cre was injected into the dmTh, AAV1-CAG-FLEX-tdTomato into SNr,
785 and AAV2retro-CAGGS-EGFP into IC. SNr axon terminals (tdTomato, red) were apposed to
786 the somata of IC-projecting dmTh neurons (EGFP, green), particularly within the rITN. White

787 rectangles in the thalamic regions in the top-right panels (scale bars, 500 μm) indicate areas
788 shown at higher magnification in the bottom-right panels (scale bars, 50 μm), highlighting these
789 appositions.
790 Abbreviations: Cla, claustrum; cp, cerebral peduncle; En, endopiriform nucleus; HPC,
791 hippocampus; ic, internal capsule; LD, laterodorsal thalamic nucleus; mPFC, medial prefrontal
792 cortex; Rh, rhomboid thalamic nucleus; S2, secondary somatosensory cortex; VP, ventral
793 pallidum; ZI, zona incerta.
794 See also Figure S2.
795
796 **Figure 5. Chemogenetic inhibition of the thalamo-insular pathway alleviates tic-like**
797 **movements**
798 (A and B) Schematics of the experimental setup for chemogenetic inhibition of IC or the dmTh-
799 IC pathway. To inhibit IC, AAV8-hSyn-hM4Di-mCherry (or control AAV8-hSyn-mCherry)
800 was bilaterally injected into three rostrocaudally distinct IC sites. To specifically inhibit the
801 thalamo-insular pathway, AAV2retro-CAGGS-Cre was bilaterally injected into IC and AAV-
802 DJ-EF1α-DIO-hM4Di-mCherry (or control AAV-DJ-EF1α-DIO-mCherry) into bilateral dmTh.
803 (C and D) Representative coronal sections showing hM4Di-mCherry-expression in IC (C) or
804 in dmTh and IC (D). Scale bars, 500 μm.
805 (E) Experimental timeline. Mice received repeated unilateral bicuculline injections into the
806 dSTR via a chronically implanted guide cannula, following intraperitoneal administration of
807 vehicle (1st test), clozapine-N-oxide (CNO, 10 mg/kg; 2nd test), and vehicle (3rd test).
808 (F and G) Chemogenetic inhibition of bilateral IC reduced both tic frequency (F) and tic
809 intensity (G) during the 30-min period after bicuculline injection (n = 8 mice).
810 (H and I) Chemogenetic inhibition of bilateral dmTh-IC pathways reduced tic intensity (I), but

811 not tic frequency (H) (n = 8 mice).

812 (J-M) Control experiment using mCherry-expressing viruses in bilateral IC (J, K) or bilateral
813 dmTh-IC pathways (L, M) showed no effects of CNO administration. (n = 8 mice for each
814 group).

815 (F-M) Data are presented as mean ± SEM; individual mouse data are shown as gray
816 circles. Statistical analyses were performed using one-way repeated measures ANOVA
817 followed by pairwise *t*-tests with Holm correction (F, H, J, and L) or one-sample *t*-tests with
818 Holm correction (G, I, K, and M). ns, not significant; **p < 0.01; ***p < 0.001.

819 See also Video S2.

820

821 **Figure 6. Chemogenetic inhibition of the thalamo-insular pathway alters downstream tic-**
822 **associated cortical activity**

823 (A) Schematic of the experimental setup for fiber photometry recording during chemogenetic
824 inhibition of the dmTh-IC pathway. To inhibit this pathway, AAV2retro-CAGGS-Cre was
825 bilaterally injected into IC, and AAV-DJ-EF1α-DIO-hM4Di-mCherry (or control AAV-DJ-
826 EF1α-DIO-mCherry) into bilateral dmTh. AAV1-Syn-GCaMP6f was injected into the
827 ipsilateral M1 and bilateral IC for fiber photometry recordings. Following implantation of a
828 guide cannula and optical fibers, tic-like movements were induced by repeated unilateral
829 bicuculline injections into the dSTR under vehicle (1st test), CNO (10 mg/kg; 2nd test), and
830 vehicle (3rd test) conditions.

831 (B) Representative traces of Ca^{2+} signals in the ipsilateral M1, ipsilateral IC, and contralateral
832 IC, together with wrist and mouth-corner movement speeds, following unilateral bicuculline
833 injection during vehicle (left) and CNO (right) sessions.

834 (C) Averaged tic-aligned Ca^{2+} signals in the ipsilateral M1, ipsilateral IC, and contralateral IC,

across the three sessions (n = 8 mice). Shaded areas represent mean ± SEM.

(D) Quantification of tic-related Ca^{2+} amplitudes in the ipsilateral M1, ipsilateral IC, and the contralateral IC (n = 8 mice). Chemogenetic inhibition of the dmTh-IC pathway significantly reduced Ca^{2+} amplitudes in the ipsilateral M1 and ipsilateral IC, but not in the contralateral IC. Data are presented as mean ± SEM; individual mouse data are shown as gray circles. Statistical analyses were performed using one-way repeated measures ANOVA followed by pairwise *t*-tests with Holm correction. ns, not significant; *$p < 0.05$.

See also Figures S3-S5.

REFERENCES

1. *Diagnostic and statistical manual of mental disorders : DSM-5-TR*. (2022). (American Psychiatric Association Publishing). 10.1176/appi.books.9780890425787.
2. Bullen, J.G., and Hemsley, D.R. (1983). Sensory experience as a trigger in Gilles de la Tourette's syndrome. J Behav Ther Exp Psychiatry *14*, 197-201. 10.1016/0005-7916(83)90048-4.
3. Kurlan, R., Lichter, D., and Hewitt, D. (1989). Sensory tics in Tourette's syndrome. Neurology *39*, 731-734. 10.1212/wnl.39.5.731.
4. Leckman, J.F., Walker, D.E., and Cohen, D.J. (1993). Premonitory urges in Tourette's syndrome. Am J Psychiatry *150*, 98-102. 10.1176/ajp.150.1.98.
5. Houghton, D.C., Capriotti, M.R., Conelea, C.A., and Woods, D.W. (2014). Sensory Phenomena in Tourette Syndrome: Their Role in Symptom Formation and Treatment. Curr Dev Disord Rep *1*, 245-251. 10.1007/s40474-014-0026-2.
6. Jankovic, J. (2001). Tourette's syndrome. N Engl J Med *345*, 1184-1192. 10.1056/NEJMra010032.
7. Leckman, J.F. (2002). Tourette's syndrome. Lancet *360*, 1577-1586. 10.1016/S0140-6736(02)11526-1.
8. Johnson, K.A., Worbe, Y., Foote, K.D., Butson, C.R., Gunduz, A., and Okun, M.S. (2023). Tourette syndrome: clinical features, pathophysiology, and treatment. Lancet Neurol *22*, 147-158. 10.1016/S1474-4422(22)00303-9.
9. Robertson, M.M. (2008). The prevalence and epidemiology of Gilles de la Tourette syndrome. Part 1: the epidemiological and prevalence studies. J Psychosom Res *65*, 461-472. 10.1016/j.jpsychores.2008.03.006.
10. Knight, T., Steeves, T., Day, L., Lowerison, M., Jette, N., and Pringsheim, T. (2012). Prevalence of tic disorders: a systematic review and meta-analysis. Pediatr Neurol *47*, 77-90. 10.1016/j.pediatrneurol.2012.05.002.
11. Scharf, J.M., Miller, L.L., Gauvin, C.A., Alabiso, J., Mathews, C.A., and Ben-Shlomo, Y. (2015). Population prevalence of Tourette syndrome: a systematic review and meta-analysis. Mov Disord *30*, 221-228. 10.1002/mds.26089.
12. Jafari, F., Abbasi, P., Rahmati, M., Hodhodi, T., and Kazeminia, M. (2022). Systematic Review and Meta-Analysis of Tourette Syndrome Prevalence; 1986 to 2022. Pediatr Neurol *137*, 6-16. 10.1016/j.pediatrneurol.2022.08.010.
13. Seideman, M.F., and Seideman, T.A. (2020). A Review of the Current Treatment of Tourette Syndrome. J Pediatr Pharmacol Ther *25*, 401-412. 10.5863/1551-6776-25.5.401.
14. Yael, D., Israelashvili, M., and Bar-Gad, I. (2016). Animal Models of Tourette Syndrome-From Proliferation to Standardization. Front Neurosci *10*, 132. 10.3389/fnins.2016.00132.

15. Tarsy, D., Pycock, C.J., Meldrum, B.S., and Marsden, C.D. (1978). Focal contralateral myoclonus produced by inhibition of GABA action in the caudate nucleus of rats. Brain *101*, 143-162. 10.1093/brain/101.1.143.

16. Bronfeld, M., Yael, D., Belelovsky, K., and Bar-Gad, I. (2013). Motor tics evoked by striatal disinhibition in the rat. Front Syst Neurosci *7*, 50. 10.3389/fnsys.2013.00050.

17. Crossman, A.R., Mitchell, I.J., Sambrook, M.A., and Jackson, A. (1988). Chorea and myoclonus in the monkey induced by gamma-aminobutyric acid antagonism in the lentiform complex. The site of drug action and a hypothesis for the neural mechanisms of chorea. Brain *111 (Pt 5)*, 1211-1233. 10.1093/brain/111.5.1211.

18. McCairn, K.W., Bronfeld, M., Belelovsky, K., and Bar-Gad, I. (2009). The neurophysiological correlates of motor tics following focal striatal disinhibition. Brain *132*, 2125-2138. 10.1093/brain/awp142.

19. Worbe, Y., Baup, N., Grabli, D., Chaigneau, M., Mounayar, S., McCairn, K., Féger, J., and Tremblay, L. (2009). Behavioral and movement disorders induced by local inhibitory dysfunction in primate striatum. Cereb Cortex *19*, 1844-1856. 10.1093/cercor/bhn214.

20. Kawaguchi, Y., Wilson, C.J., Augood, S.J., and Emson, P.C. (1995). Striatal interneurones: chemical, physiological and morphological characterization. Trends Neurosci *18*, 527-535. 10.1016/0166-2236(95)98374-8.

21. Kalanithi, P.S., Zheng, W., Kataoka, Y., DiFiglia, M., Grantz, H., Saper, C.B., Schwartz, M.L., Leckman, J.F., and Vaccarino, F.M. (2005). Altered parvalbumin-positive neuron distribution in basal ganglia of individuals with Tourette syndrome. Proc Natl Acad Sci U S A *102*, 13307-13312. 10.1073/pnas.0502624102.

22. Kataoka, Y., Kalanithi, P.S., Grantz, H., Schwartz, M.L., Saper, C., Leckman, J.F., and Vaccarino, F.M. (2010). Decreased number of parvalbumin and cholinergic interneurons in the striatum of individuals with Tourette syndrome. J Comp Neurol *518*, 277-291. 10.1002/cne.22206.

23. Shapiro, E., Shapiro, A.K., Fulop, G., Hubbard, M., Mandeli, J., Nordlie, J., and Phillips, R.A. (1989). Controlled study of haloperidol, pimozide and placebo for the treatment of Gilles de la Tourette's syndrome. Arch Gen Psychiatry *46*, 722-730. 10.1001/archpsyc.1989.01810080052006.

24. Kelley, A.E., Lang, C.G., and Gauthier, A.M. (1988). Induction of oral stereotypy following amphetamine microinjection into a discrete subregion of the striatum. Psychopharmacology (Berl) *95*, 556-559. 10.1007/BF00172976.

25. Conceição, V.A., Dias, Â., Farinha, A.C., and Maia, T.V. (2017). Premonitory urges and tics in Tourette syndrome: computational mechanisms and neural correlates. Curr Opin Neurobiol *46*, 187-199. 10.1016/j.conb.2017.08.009.

26. Jackson, S.R., Loayza, J., Crighton, M., Sigurdsson, H.P., Dyke, K., and Jackson, G.M. (2020).

The role of the insula in the generation of motor tics and the experience of the premonitory urge-to-tic in Tourette syndrome. Cortex *126*, 119-133. 10.1016/j.cortex.2019.12.021.

27. Bohlhalter, S., Goldfine, A., Matteson, S., Garraux, G., Hanakawa, T., Kansaku, K., Wurzman, R., and Hallett, M. (2006). Neural correlates of tic generation in Tourette syndrome: an event-related functional MRI study. Brain *129*, 2029-2037. 10.1093/brain/awl050.

28. Lerner, A., Bagic, A., Boudreau, E.A., Hanakawa, T., Pagan, F., Mari, Z., Bara-Jimenez, W., Aksu, M., Garraux, G., Simmons, J.M., et al. (2007). Neuroimaging of neuronal circuits involved in tic generation in patients with Tourette syndrome. Neurology *68*, 1979-1987. 10.1212/01.wnl.0000264417.18604.12.

29. Lee, J., Wang, W., and Sabatini, B.L. (2020). Anatomically segregated basal ganglia pathways allow parallel behavioral modulation. Nat Neurosci *23*, 1388-1398. 10.1038/s41593-020-00712-5.

30. Foster, N.N., Barry, J., Korobkova, L., Garcia, L., Gao, L., Becerra, M., Sherafat, Y., Peng, B., Li, X., Choi, J.H., et al. (2021). The mouse cortico-basal ganglia-thalamic network. Nature *598*, 188-194. 10.1038/s41586-021-03993-3.

31. McElvain, L.E., Chen, Y., Moore, J.D., Brigidi, G.S., Bloodgood, B.L., Lim, B.K., Costa, R.M., and Kleinfeld, D. (2021). Specific populations of basal ganglia output neurons target distinct brain stem areas while collateralizing throughout the diencephalon. Neuron *109*, 1721-1738.e1724. 10.1016/j.neuron.2021.03.017.

32. Aoki, S., Smith, J.B., Li, H., Yan, X., Igarashi, M., Coulon, P., Wickens, J.R., Ruigrok, T.J., and Jin, X. (2019). An open cortico-basal ganglia loop allows limbic control over motor output via the nigrothalamic pathway. Elife *8*. 10.7554/eLife.49995.

33. Hariz, M.I., and Robertson, M.M. (2010). Gilles de la Tourette syndrome and deep brain stimulation. Eur J Neurosci *32*, 1128-1134. 10.1111/j.1460-9568.2010.07415.x.

34. Arnts, H., Coolen, S.E., Fernandes, F.W., Schuurman, R., Krauss, J.K., Groenewegen, H.J., and van den Munckhof, P. (2023). The intralaminar thalamus: a review of its role as a target in functional neurosurgery. Brain Commun *5*, fcad003. 10.1093/braincomms/fcad003.

35. Manvich, D.F., Webster, K.A., Foster, S.L., Farrell, M.S., Ritchie, J.C., Porter, J.H., and Weinshenker, D. (2018). The DREADD agonist clozapine N-oxide (CNO) is reverse-metabolized to clozapine and produces clozapine-like interoceptive stimulus effects in rats and mice. Sci Rep *8*, 3840. 10.1038/s41598-018-22116-z.

36. Rodd, Z.A., Engleman, E.A., Truitt, W.A., Burke, A.R., Molosh, A.I., Bell, R.L., and Hauser, S.R. (2022). CNO Administration Increases Dopamine and Glutamate in the Medial Prefrontal Cortex of Wistar Rats: Further Concerns for the Validity of the CNO-activated DREADD Procedure. Neuroscience *491*, 176-184. 10.1016/j.neuroscience.2022.03.028.

37. Scharf, J.M., Yu, D., Mathews, C.A., Neale, B.M., Stewart, S.E., Fagerness, J.A., Evans, P.,

952 Gamazon, E., Edlund, C.K., Service, S.K., et al. (2013). Genome-wide association study of
953 Tourette's syndrome. Mol Psychiatry *18*, 721-728. 10.1038/mp.2012.69.
954 38. Willsey, A.J., Fernandez, T.V., Yu, D., King, R.A., Dietrich, A., Xing, J., Sanders, S.J., Mandell,
955 J.D., Huang, A.Y., Richer, P., et al. (2017). De Novo Coding Variants Are Strongly Associated
956 with Tourette Disorder. Neuron *94*, 486-499.e489. 10.1016/j.neuron.2017.04.024.
957 39. Lu, Q., Zhou, Y., Qian, Q., Chen, Z., Tan, Q., Chen, H., Yin, F., Wang, Y., Liu, Z., Tian, P., and
958 Sun, D. (2024). Whole-exome sequencing identifies high-confidence genes for tic disorders in a
959 Chinese Han population. Clin Chim Acta *561*, 119759. 10.1016/j.cca.2024.119759.
960 40. Kowalski, T.F., Wang, R., and Tischfield, M.A. (2025). Genetic advances and translational
961 phenotypes in rodent models for Tourette disorder. Curr Opin Neurobiol *90*, 102967.
962 10.1016/j.conb.2024.102967.
963 41. Godar, S.C., Mosher, L.J., Di Giovanni, G., and Bortolato, M. (2014). Animal models of tic
964 disorders: a translational perspective. J Neurosci Methods *238*, 54-69.
965 10.1016/j.jneumeth.2014.09.008.
966 42. McCairn, K.W., Nagai, Y., Hori, Y., Ninomiya, T., Kikuchi, E., Lee, J.Y., Suhara, T., Iriki, A.,
967 Minamimoto, T., Takada, M., et al. (2016). A Primary Role for Nucleus Accumbens and Related
968 Limbic Network in Vocal Tics. Neuron *89*, 300-307. 10.1016/j.neuron.2015.12.025.
969 43. Gittis, A.H., Berke, J.D., Bevan, M.D., Chan, C.S., Mallet, N., Morrow, M.M., and Schmidt, R.
970 (2014). New roles for the external globus pallidus in basal ganglia circuits and behavior. J
971 Neurosci *34*, 15178-15183. 10.1523/JNEUROSCI.3252-14.2014.
972 44. Matsumura, M., Tremblay, L., Richard, H., and Filion, M. (1995). Activity of pallidal neurons in
973 the monkey during dyskinesia induced by injection of bicuculline in the external pallidum.
974 Neuroscience *65*, 59-70. 10.1016/0306-4522(94)00484-m.
975 45. Grabli, D., McCairn, K., Hirsch, E.C., Agid, Y., Féger, J., François, C., and Tremblay, L. (2004).
976 Behavioural disorders induced by external globus pallidus dysfunction in primates: I. Behavioural
977 study. Brain *127*, 2039-2054. 10.1093/brain/awh220.
978 46. Bronfeld, M., Belelovsky, K., Erez, Y., Bugaysen, J., Korngreen, A., and Bar-Gad, I. (2010).
979 Bicuculline-induced chorea manifests in focal rather than globalized abnormalities in the
980 activation of the external and internal globus pallidus. J Neurophysiol *104*, 3261-3275.
981 10.1152/jn.00093.2010.
982 47. Tachibana, Y., Kita, H., Chiken, S., Takada, M., and Nambu, A. (2008). Motor cortical control
983 of internal pallidal activity through glutamatergic and GABAergic inputs in awake monkeys. Eur
984 J Neurosci *27*, 238-253. 10.1111/j.1460-9568.2007.05990.x.
985 48. McCairn, K.W., Iriki, A., and Isoda, M. (2013). Global dysrhythmia of cerebro-basal ganglia-
986 cerebellar networks underlies motor tics following striatal disinhibition. J Neurosci *33*, 697-708.
987 10.1523/JNEUROSCI.4018-12.2013.

988 49. Murakami, J., Tachibana, Y., Akiyama, S., Kato, T., Taniguchi, A., Nakajima, Y., Shimoda, M.,
989 Wake, H., Kano, Y., Takada, M., et al. (2019). Oral splint ameliorates tic symptoms in patients
990 with tourette syndrome. Mov Disord *34*, 1577-1578. 10.1002/mds.27819.
991 50. Yoshida, A., Fujio, T., Sato, F., Ali, M.S.S., Haque, T., Ohara, H., Moritani, M., Kato, T.,
992 Dostrovsky, J.O., and Tachibana, Y. (2017). Orofacial proprioceptive thalamus of the rat. Brain
993 Struct Funct *222*, 2655-2669. 10.1007/s00429-016-1363-1.
994 51. Sato, F., Uemura, Y., Kanno, C., Tsutsumi, Y., Tomita, A., Oka, A., Kato, T., Uchino, K.,
995 Murakami, J., Haque, T., et al. (2017). Thalamo-insular pathway conveying orofacial muscle
996 proprioception in the rat. Neuroscience *365*, 158-178. 10.1016/j.neuroscience.2017.09.050.
997 52. Craig, A.D. (2002). How do you feel? Interoception: the sense of the physiological condition of
998 the body. Nat Rev Neurosci *3*, 655-666. 10.1038/nrn894.
999 53. Craig, A.D. (2009). How do you feel--now? The anterior insula and human awareness. Nat Rev
1000 Neurosci *10*, 59-70. 10.1038/nrn2555.
1001 54. Namkung, H., Kim, S.H., and Sawa, A. (2017). The Insula: An Underestimated Brain Area in
1002 Clinical Neuroscience, Psychiatry, and Neurology. Trends Neurosci *40*, 200-207.
1003 10.1016/j.tins.2017.02.002.
1004 55. Bergman, H., Wichmann, T., and DeLong, M.R. (1990). Reversal of experimental parkinsonism
1005 by lesions of the subthalamic nucleus. Science *249*, 1436-1438. 10.1126/science.2402638.
1006 56. Lozano, A.M., Lang, A.E., Galvez-Jimenez, N., Miyasaki, J., Duff, J., Hutchinson, W.D., and
1007 Dostrovsky, J.O. (1995). Effect of GPi pallidotomy on motor function in Parkinson's disease.
1008 Lancet *346*, 1383-1387. 10.1016/s0140-6736(95)92404-3.
1009 57. Lang, A.E., and Lozano, A.M. (1998). Parkinson's disease. First of two parts. N Engl J Med *339*,
1010 1044-1053. 10.1056/NEJM199810083391506.
1011 58. Boraud, T., Bezard, E., Bioulac, B., and Gross, C. (1996). High frequency stimulation of the
1012 internal Globus Pallidus (GPi) simultaneously improves parkinsonian symptoms and reduces
1013 the firing frequency of GPi neurons in the MPTP-treated monkey. Neurosci Lett *215*, 17-20.
1014 10.1016/s0304-3940(96)12943-8.
1015 59. Obeso, J.A., Olanow, C.W., Rodriguez-Oroz, M.C., Krack, P., Kumar, R., Lang, A.E., and Group,
1016 D.-B.S.f.P.s.D.S. (2001). Deep-brain stimulation of the subthalamic nucleus or the pars interna
1017 of the globus pallidus in Parkinson's disease. N Engl J Med *345*, 956-963.
1018 10.1056/NEJMoa000827.
1019 60. Lozano, A.M., Lipsman, N., Bergman, H., Brown, P., Chabardes, S., Chang, J.W., Matthews, K.,
1020 McIntyre, C.C., Schlaepfer, T.E., Schulder, M., et al. (2019). Deep brain stimulation: current
1021 challenges and future directions. Nat Rev Neurol *15*, 148-160. 10.1038/s41582-018-0128-2.
1022 61. Vandewalle, V., van der Linden, C., Groenewegen, H.J., and Caemaert, J. (1999). Stereotactic
1023 treatment of Gilles de la Tourette syndrome by high frequency stimulation of thalamus. Lancet

353, 724. 10.1016/s0140-6736(98)05964-9.

62. Singer, H.S. (2005). Tourette's syndrome: from behaviour to biology. Lancet Neurol *4*, 149-159. 10.1016/S1474-4422(05)01012-4.

63. Sadikot, A.F., and Rymar, V.V. (2009). The primate centromedian-parafascicular complex: anatomical organization with a note on neuromodulation. Brain Res Bull *78*, 122-130. 10.1016/j.brainresbull.2008.09.016.

64. Cover, K.K., and Mathur, B.N. (2021). Rostral Intralaminar Thalamus Engagement in Cognition and Behavior. Front Behav Neurosci *15*, 652764. 10.3389/fnbeh.2021.652764.

65. Alexander, G.E., DeLong, M.R., and Strick, P.L. (1986). Parallel organization of functionally segregated circuits linking basal ganglia and cortex. Annu Rev Neurosci *9*, 357-381. 10.1146/annurev.ne.09.030186.002041.

66. Alexander, G.E., and Crutcher, M.D. (1990). Functional architecture of basal ganglia circuits: neural substrates of parallel processing. Trends Neurosci *13*, 266-271. 10.1016/0166-2236(90)90107-l.

67. Tremblay, L., Worbe, Y., Thobois, S., Sgambato-Faure, V., and Féger, J. (2015). Selective dysfunction of basal ganglia subterritories: From movement to behavioral disorders. Mov Disord *30*, 1155-1170. 10.1002/mds.26199.

68. Papez, J. (1937). A proposed mechanism of emotion. Archives of Neurology and Psychiatry *38*, 725-743. 10.1001/archneurpsyc.1937.02260220069003.

69. Saper, C.B. (1982). Convergence of autonomic and limbic connections in the insular cortex of the rat. J Comp Neurol *210*, 163-173. 10.1002/cne.902100207.

70. Fudge, J.L., Breitbart, M.A., Danish, M., and Pannoni, V. (2005). Insular and gustatory inputs to the caudal ventral striatum in primates. J Comp Neurol *490*, 101-118. 10.1002/cne.20660.

71. Gehrlach, D.A., Weiand, C., Gaitanos, T.N., Cho, E., Klein, A.S., Hennrich, A.A., Conzelmann, K.K., and Gogolla, N. (2020). A whole-brain connectivity map of mouse insular cortex. Elife *9*. 10.7554/eLife.55585.

72. Tyler, W.J., Lani, S.W., and Hwang, G.M. (2018). Ultrasonic modulation of neural circuit activity. Curr Opin Neurobiol *50*, 222-231. 10.1016/j.conb.2018.04.011.

73. Rabut, C., Yoo, S., Hurt, R.C., Jin, Z., Li, H., Guo, H., Ling, B., and Shapiro, M.G. (2020). Ultrasound Technologies for Imaging and Modulating Neural Activity. Neuron *108*, 93-110. 10.1016/j.neuron.2020.09.003.

74. Martínez-Fernández, R., Paschen, S., Del Álamo, M., Rodríguez-Rojas, R., Pineda-Pardo, J.A., Blesa, J., Kaplitt, M.G., Deuschl, G., and Obeso, J.A. (2025). Focused ultrasound therapy for movement disorders. Lancet Neurol *24*, 698-712. 10.1016/S1474-4422(25)00210-8.

75. Tanahira, C., Higo, S., Watanabe, K., Tomioka, R., Ebihara, S., Kaneko, T., and Tamamaki, N. (2009). Parvalbumin neurons in the forebrain as revealed by parvalbumin-Cre transgenic mice.

Neurosci Res *63*, 213-223. 10.1016/j.neures.2008.12.007.

76. Franklin, K.B.J., and Paxinos, G. (2008). The Mouse Brain in Stereotaxic Coordinates, Compact, 3rd Edition.

77. Sotani, N., Kusuhara, S., Nishisho, R., Kuno, H., Shima, H., Haruwaka, K., Mori, Y., Kishi, M., Furuyashiki, T., Kobayashi, K., et al. Transpupillary in vivo two-photon imaging reveals enhanced surveillance of retinal microglia in diabetic mice (in press). Proc Natl Acad Sci.

78. Mathis, A., Mamidanna, P., Cury, K.M., Abe, T., Murthy, V.N., Mathis, M.W., and Bethge, M. (2018). DeepLabCut: markerless pose estimation of user-defined body parts with deep learning. Nat Neurosci *21*, 1281-1289. 10.1038/s41593-018-0209-y.

79. Kawanabe-Kobayashi, R., Uchiyama, S., Yoshihara, K., Kojima, D., McHugh, T., Hatada, I., Matsui, K., Tanaka, K.F., and Tsuda, M. (2025). Descending locus coeruleus noradrenergic signaling to spinal astrocyte subset is required for stress-induced pain facilitation (Preprint). Elife. 10.7554/elife.104453.1.

80. Spulák, D., Cmejla, R., Bačáková, R., Kračmar, B., Satrapová, L., and Novotný, P. (2014). Muscle activity detection in electromyograms recorded during periodic movements. Comput Biol Med *47*, 93-103. 10.1016/j.compbiomed.2014.01.013.

81. Cantu, D.A., Wang, B., Gongwer, M.W., He, C.X., Goel, A., Suresh, A., Kourdougli, N., Arroyo, E.D., Zeiger, W., and Portera-Cailliau, C. (2020). EZcalcium: Open-Source Toolbox for Analysis of Calcium Imaging Data. Front Neural Circuits *14*, 25. 10.3389/fncir.2020.00025.

82. Okada, T., Kato, D., Nomura, Y., Obata, N., Quan, X., Morinaga, A., Yano, H., Guo, Z., Aoyama, Y., Tachibana, Y., et al. (2021). Pain induces stable, active microcircuits in the somatosensory cortex that provide a therapeutic target. Sci Adv *7*. 10.1126/sciadv.abd8261.

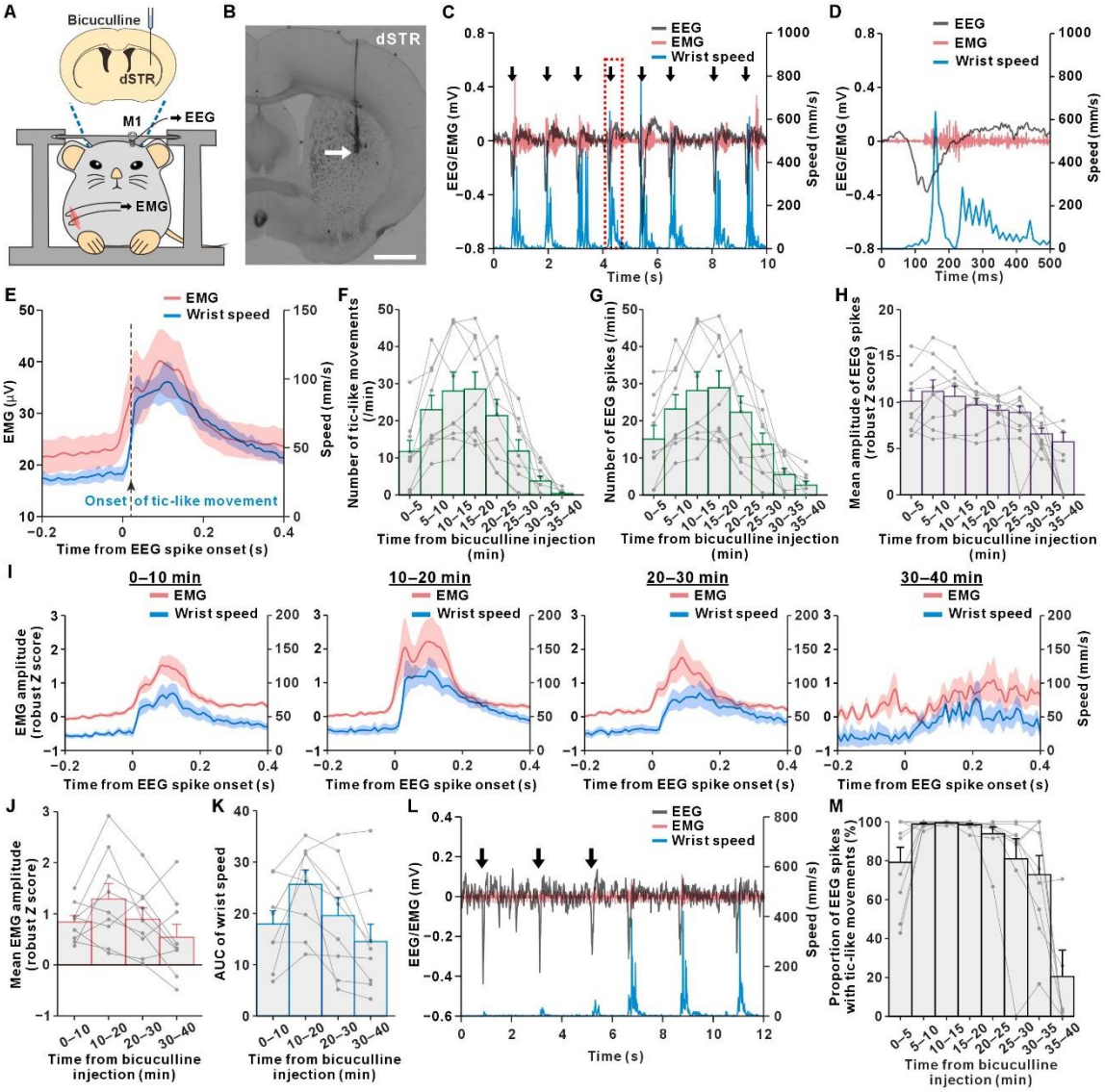

Fig. 1 Kuno et al.
(2 columns)

1083

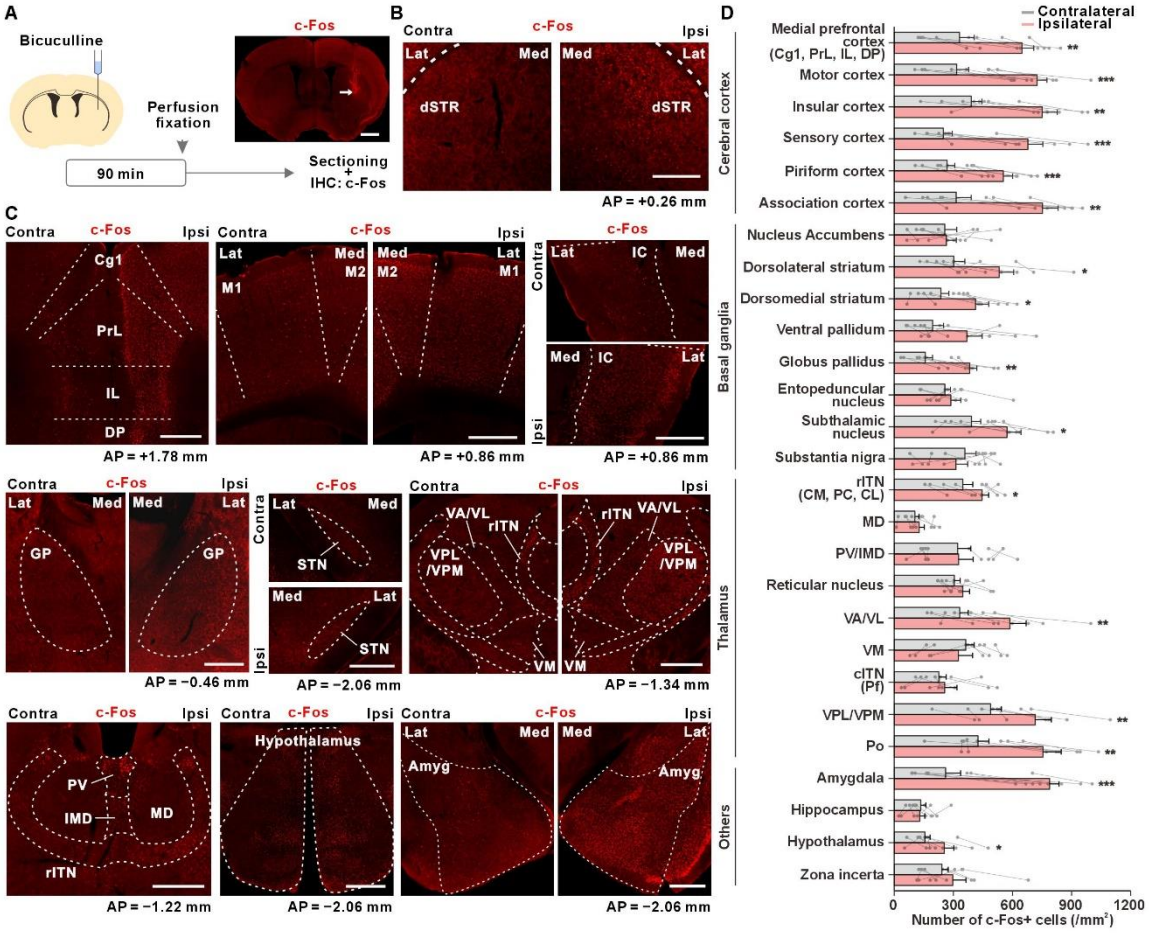

Fig. 2 Kuno et al.
(2 columns)

1084

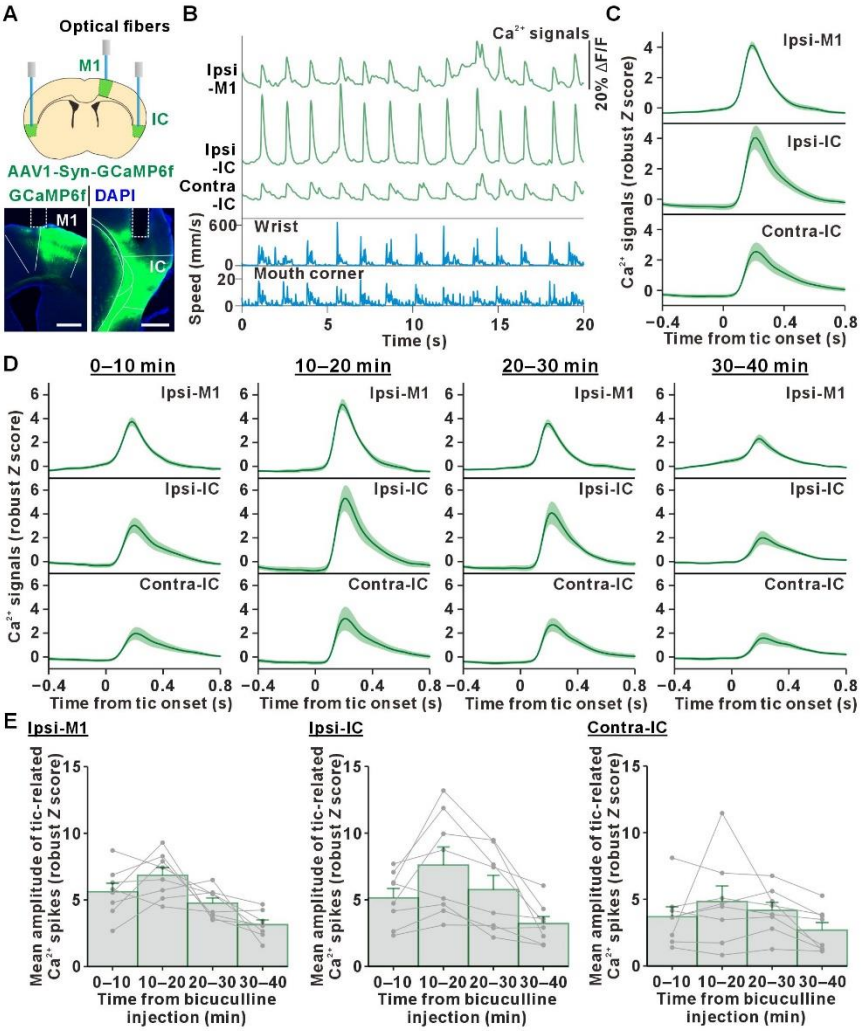

Fig. 3 Kuno et al.
(1.5 columns)

1085

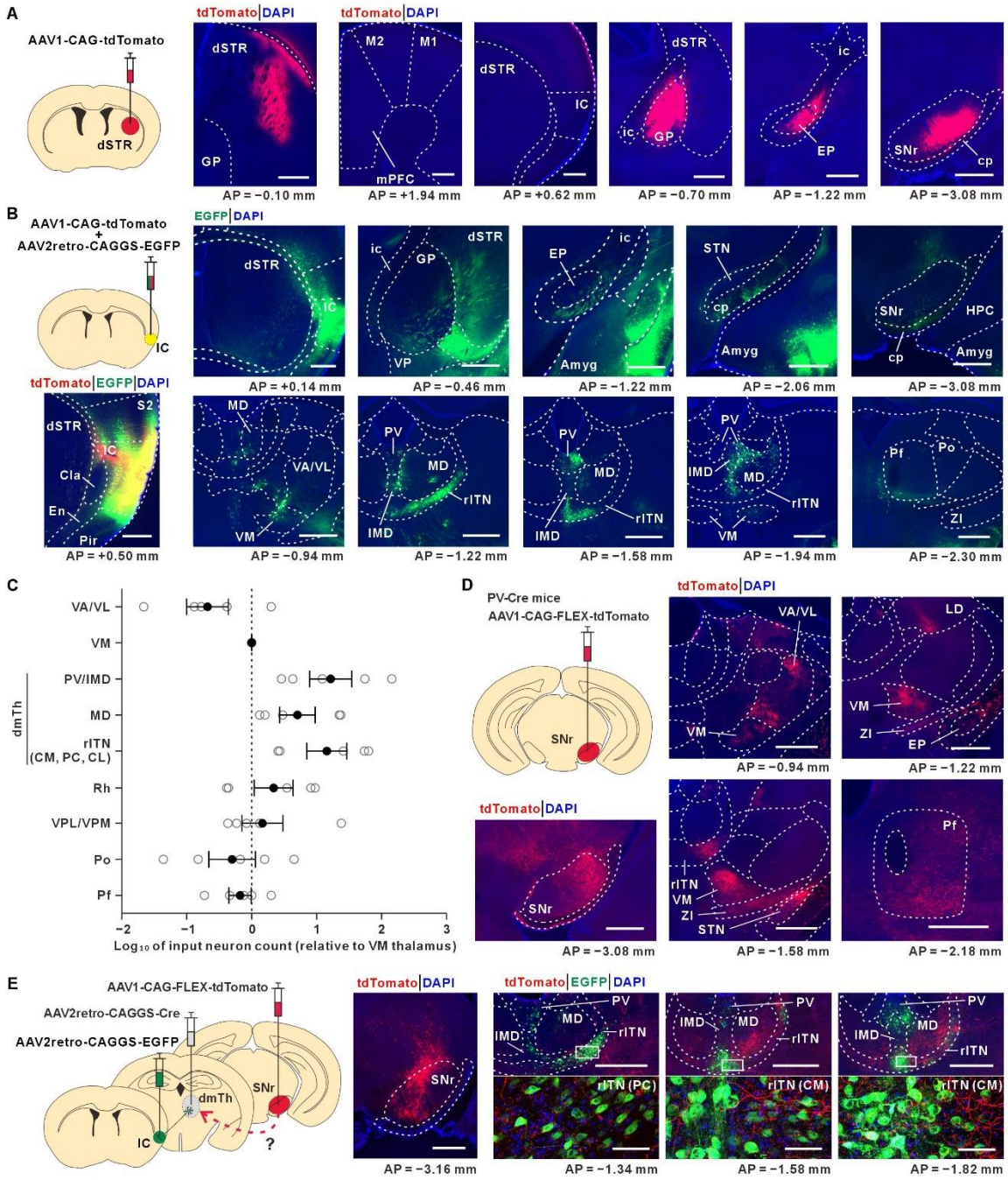

Fig. 4 Kuno et al.
(2 columns)

1086

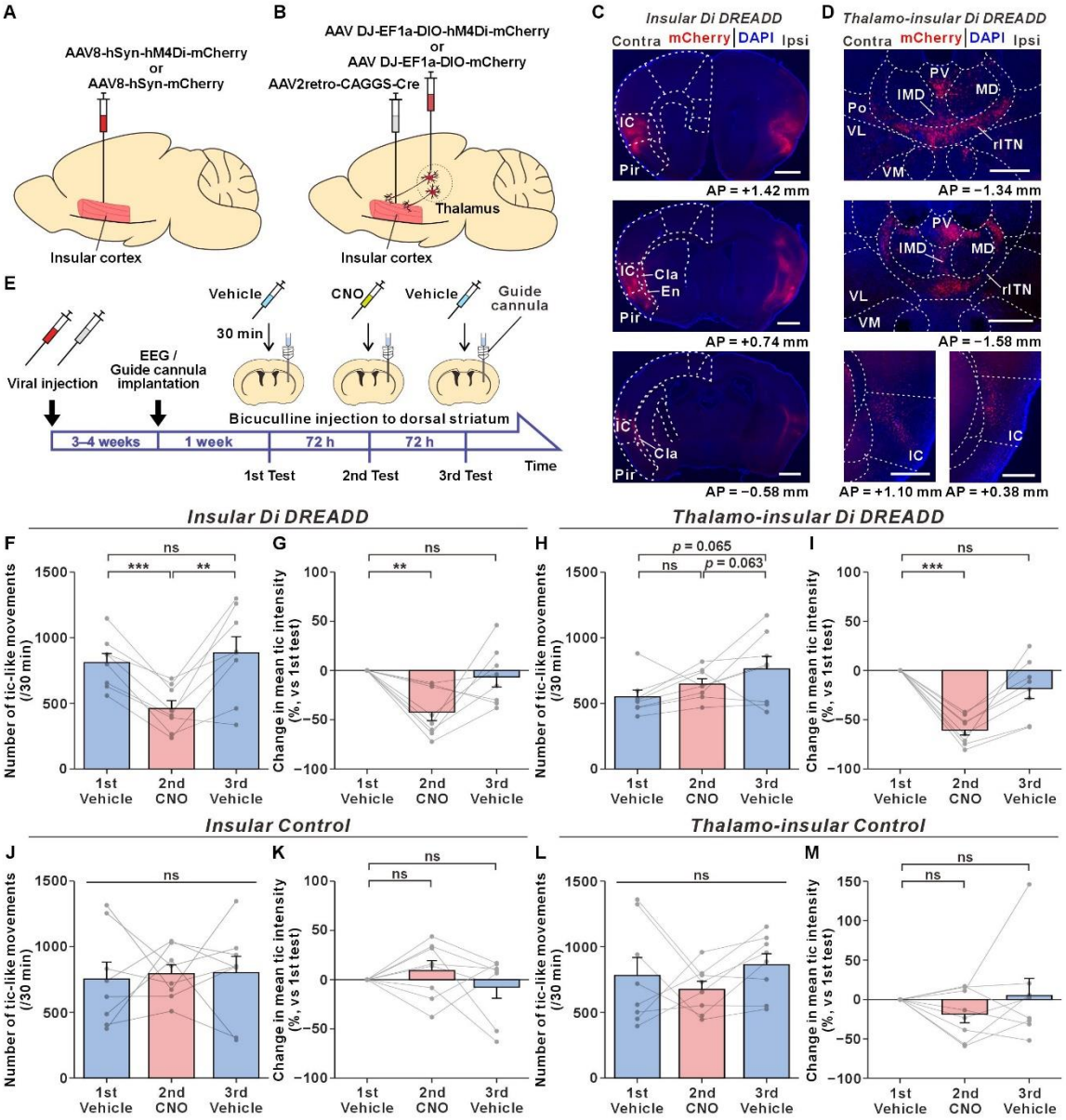

Fig. 5 Kuno et al.
(2 columns)

1087

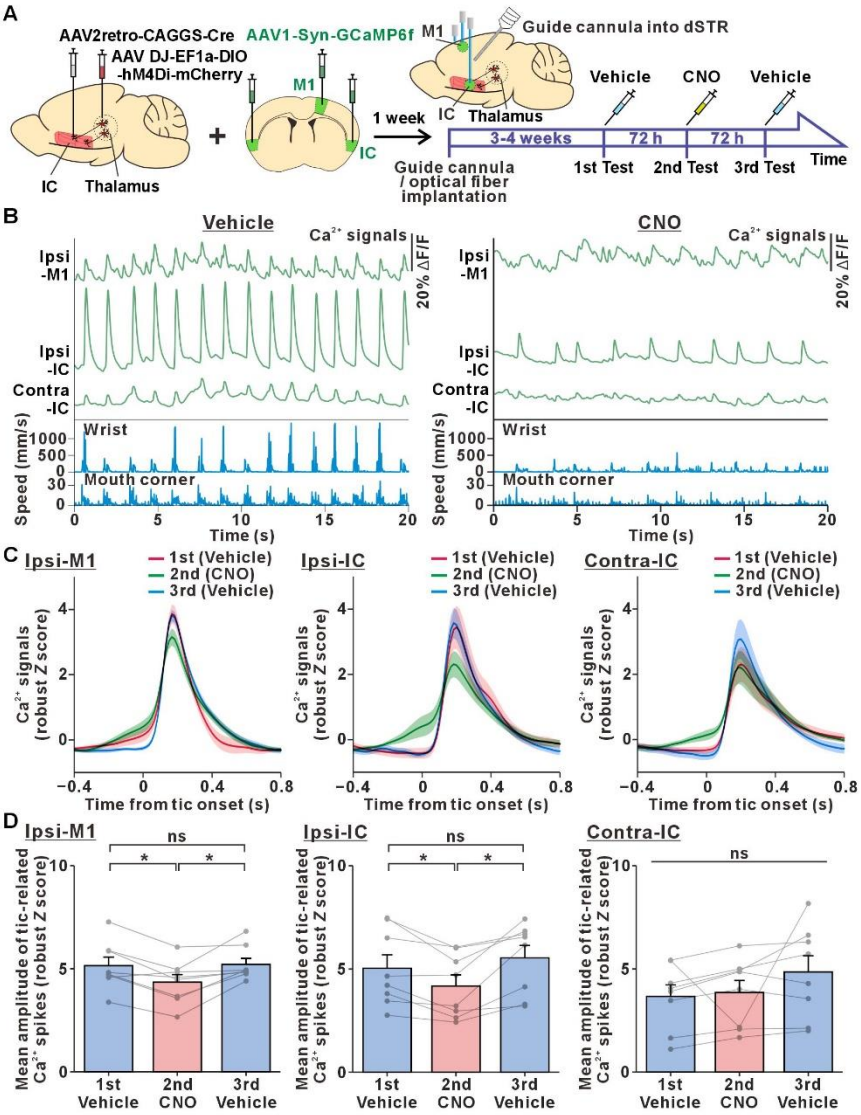

Fig. 6 Kuno et al.
(1.5 columns)

1088